Reconstructing Eocene Paleotopography of the Northern U.S. Cordillera Using Stable
Isotope Paleoaltimetry of Hydrated Volcanic Glass

Presented in Partial Fulfillment of the Requirements for the

Degree of Master of Science

with a

Major in Geology

in the

College of Graduate Studies

University of Idaho

by

Erin E. Young-Dahl

Major Professor: Elizabeth J. Cassel, PhD

Committee Members: Jessica R. Stanley, PhD; Daniel O. Breecker, PhD
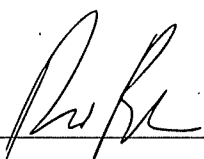
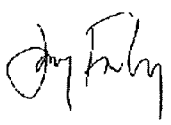Department Administrator: Jerry P. Fairley, PhD

August 2021

Authorization to Submit Thesis

This thesis of Erin E. Young-Dahl, submitted for the degree of Master of Science with a Major in Geology and titled "**Reconstructing Eocene Paleotopography of the Northern U.S. Cordillera Using Stable Isotope Paleoaltimetry of Hydrated Volcanic Glass**," has been reviewed in final form. Permission, as indicated by the signatures and dates below, is now granted to submit final copies to the College of Graduate Studies for approval.

Major Professor: _____ Date: 8/5/2021

Elizabeth J. Cassel, PhD

Committee Members: _____ Date: 8/4/2021

Jessica R. Stanley, PhD

_____ Date: 8/3/2021

Daniel O. Breecker, PhD

Department Chair: _____ Date: 8/5/2021

Jerry P. Fairley, PhD

Abstract

Topography controls regional drainage patterns, sediment transport, resource accumulation, climate, and atmospheric circulation. In turn, topography is controlled by plate tectonic forces and crust and mantle processes, such as compression, delamination, extension, heating, and magmatism. In studying the surface record, researchers can estimate past elevations, the timing of surface uplift or lowering, and the regional extent of highlands, which are needed to characterize the lithospheric processes and conditions responsible for changes in surface topography. In the complex tectonic setting of the northwestern United States, paleoelevation records can help interpret the timing and processes behind Rocky Mountain orogenesis. During the Eocene (ca. 56-34 Ma), the northern U.S. Cordillera experienced a shift from compression and Laramide-style thrusting to extension, recorded in extensional basin formation, exhumation of metamorphic core complexes, and southwestward migration of magmatic activity, accompanying surface uplift in the fold-thrust belt and elevated Sevier hinterland. However, researchers disagree on the extent, lifespan, and elevation of this highland or how the region evolved into the modern Rocky Mountains.

Stable isotope paleoaltimetry of Eocene-age hydrated volcanic glass shards, collected along a longitudinal transect from the western paleoshoreline to the Great Plains, was used to determine estimates and locations of high topography associated with Rocky Mountain surface uplift and lowering in the Paleogene. Volcanic glass hydration waters act as a proxy for the long-term average hydrogen isotopic ratio (δD_{glass}) values of paleo-meteoric water at the time of glass deposition. Fluvial and alluvial sample δD_{glass} values range from -223.6‰ ± 2.4‰ to -89.0‰ ± 6.9‰$_{VSMOW}$. The most D-depleted samples are consistently found in west-central and southwest Montana, and yield modeled paleoelevations of 4640 $^{+720}/_{-440}$ m in the early Eocene down to 3400 $^{+520}/_{-540}$ m in the late Eocene - Oligocene. These one-dimensional rainout model results show that topography was long-standing throughout the Paleogene, despite surface lowering by ~1200 m by the Oligocene. Both modern and ancient δD patterns suggest a dominant westerly moisture source and a zone of airmass mixing on the leeward side of the range. Because high Eocene pCO$_2$ would have reduced isotopic lapse rates, these values are minimum paleoelevation estimates. Tuff correlation using trace and rare earth

element analysis reveals ground and atmospheric transportation pathways to deliver volcanic materials from Challis and Absaroka volcanic fields to ponded basins in the Wyoming Laramide province. A combination of crustal thickening from recent shortening and thermal/geodynamic effects from Farallon slab rollback, delamination, and/or high heat flow from regional volcanic activity are likely responsible for the development of Paleogene northern U.S. Cordilleran paleo-highs.

Acknowledgments

Thank you to my marvelous teachers, professors, and peers, who encouraged me to take chances, make mistakes, get messy, and above all, never stop wondering.

Liz: Thank you for your infinite patience and wisdom over the last two years. I'm grateful for your help and guidance with all things life and geology and for introducing me to the wild world of stable isotopes and ancient mountain ranges. This experience has been rigorous and unforgettably wonderful.

Haley: You were there when things went badly, and you were there when things went well. Thank you for navigating all that is grad school and advanced research at my side. Your field assistance was invaluable, and I can't think of another person with whom I'd rather bottom out on a boulder!

My wonderful committee members, Jess and Dan: Thank you for your feedback on this thesis and your excellent suggestions for taking my interpretations to the next level.

Additional thanks to Dan for generously allowing me use of the stable isotope lab and the mass spectrometer. The pandemic severely shortened the timeframe of analysis and almost took away the chance to run the analyses myself. I sincerely thank you for the opportunity for me to take my research from fieldwork planning and sample collection all the way to sample analysis and interpretation of results. This has been a truly valuable experience.

Thank you to the following agencies for the funding that made this project a reality:

National Science Foundation

University of Idaho Graduate and Professional Student Association

Tobacco Root Geological Society

Society of Sedimentary Geologists Foundation

American Association of Petroleum Geologists

Geological Society of America

Dedication

For the strong women in my life: past, present, and future.

…but especially my sister.

Table of Contents

List of Figures

List of Tables

I. INTRODUCTION

The U.S. Cordillera provides an example of long-lived multi-phase plate deformation driven by Farallon plate subduction between ca. 220-40 Ma (Dickinson et al., 1988; DeCelles, 2004; Heller and Liu, 2016; Yonkee and Weil, 2015). Overlapping styles of compressional deformation, Sevier thin-skinned (120-50 Ma) and Laramide thick-skinned (80-40 Ma), created an overthickened crustal welt in the Sevier fold-thrust belt of western Montana and eastern Idaho to central Utah (Fig. 1.1; Coney and Harms, 1984; Snell et al., 2014). Beginning ca. 55 Ma, the exhumation of metamorphic core complexes, formation of extensional basins in southwest Montana, and rejuvenated magmatic activity demonstrate a shift in the dominant tectonic regime from compression to extension (Smith et al., 2014; Yonkee and Weil, 2015; Canada et al., 2019). The effects of this tectonic reorganization in have prompted debate on the topographic response to changing stress fields, thermal weakening, delamination, and Farallon slab removal (e.g., Coney and Harms, 1984; Janecke et al., 1994; Constenius, 1996; Blankenau, 1999; Sonder and Jones, 1999; DeCelles, 2004; Smith et al., 2014; Humphreys, 2015; Chamberlain, 2012; Karlstrom, 2012; Fan et al., 2014; 2021; Cassel et al., 2014; 2018).

The hypotheses for the timing, magnitude, and mechanisms of surface uplift of northern U.S. Cordilleran peak elevations are diverse (DeCelles, 2004; Snell et al., 2014; Fan et al., 2021). Many researchers asserted that the highest paleoelevations were in the Sevier fold thrust belt, accompanied by the development an Andean-style high plateau (2-4 km elevations) in the late Cretaceous to early Eocene Sevier hinterland (Coney and Harms, 1984; DeCelles, 2004; Snell et al., 2014; Cassel et al., 2018; Schwartz et al., 2019; Canada et al., 2019). Other hypotheses attribute kilometer-scale surface uplift to high heat flow or dynamic topography during proposed Eocene Farallon slab rollback or crustal delamination in the Eocene (SWEEP model of Chamberlain et al., 2012; Fan et al., 2014; Humphreys, 2015; Heller and Liu, 2016). Some workers also support younger uplift models, claiming that 25-50% (0.5-1.5 km) of modern Rocky Mountain high topography was attained in the Neogene through tilting or thermal uplift (Dickinson et al., 1988; Heller et al., 2003; 2016; McMillan et al., 2006; Karlstrom et al., 2012; Levandowski et al., 2018). To form a unifying hypothesis reconstructing the tectonomagmatic conditions of the northern U.S. Cordillera requires quantification of Paleogene surface elevations (Chamberlain et al., 2012).
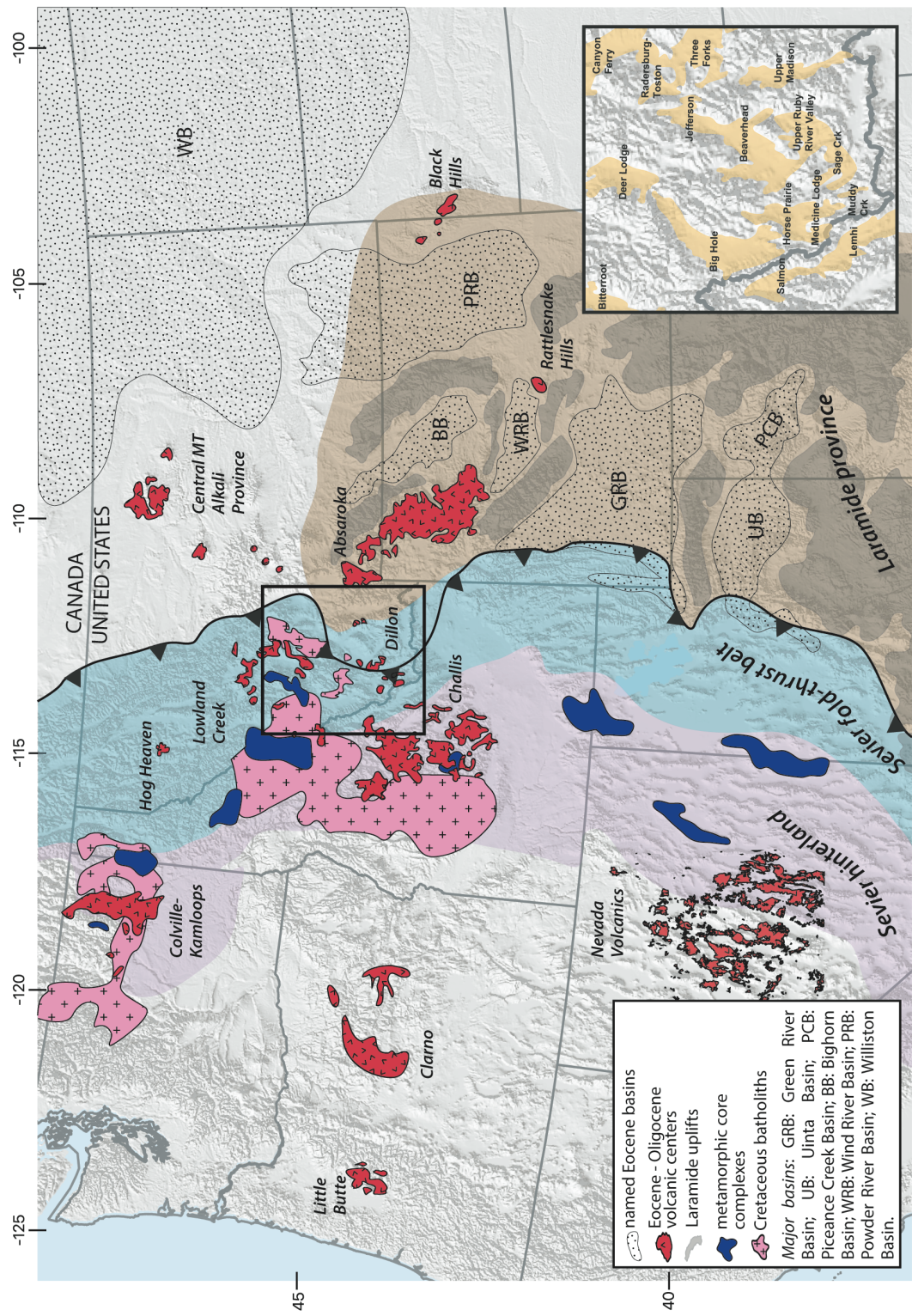
Figure 1.1. Regional map of study area with key geologic features and tectonic provinces highlighted. Volcanic centers and basins identified by name. *INSET*: Map of basins in southwest and west-central Montana.

In this study, ^{2}H/^{1}H ratios of hydration waters preserved in felsic volcanic glass (δD_{glass}) are used to paleoelevations across the northern US Cordilleran hinterland, fold-thrust belt, and foreland basin from 58 – 26 Ma. Though researchers have used stable isotope paleoaltimetry with a variety of proxies to estimate northern Rocky Mountain paleoelevations (e.g., detachment zone muscovites of Mulch, 2007; pedogenic carbonates of Schwartz et al., 2019), the large spatial extent of this study enables an assessment of broader topographic trends. The locations and magnitudes of the highest mean paleoelevations across the transect provide needed constraints for geodynamic models using tectonic and mantle condition parameters. In addition to paleoelevation estimates, this study combines geochemical correlations based on regional tephrochronology with modeled paleoelevations and modern water comparisons to assess the changes in topography throughout the Cenozoic creating a timeline of peak elevations and identifying drainage pathways and atmospheric circulation patterns (Mulch et al., 2004; Mix et al., 2011; Cassel et al., 2012; 2014; Fan et al., 2014). The new δD_{glass} values record early Eocene high elevations of 4640 $^{+720}/_{-440}$ m in west-central and southwest Montana at the toe of the Sevier fold-thrust belt, Based on the results of a climate-calibrated one-dimensional rainout model (Rowley et al., 2001). These elevations may have been created and supported through a combination of crustal thickening and Farallon slab rollback- and/or delamination-related surface uplift or lowering components.

2. GEOLOGIC BACKGROUND

2.1. Mesozoic-Cenozoic Tectonic Setting

The subduction of the oceanic Farallon tectonic plate beneath the North American plate resulted in both Sevier thin-skinned and Laramide thick-skinned deformation and crustal thickening (ca. 120-40 Ma). Thin-skinned thrusting and continental arc magmatism characterize subduction-related processes within the Sevier orogenic belt (DeCelles, 2004). Progressive eastward migration of magmatism from 80 – 55 Ma provides evidence of a shallowing angle of subduction of the Farallon plate during the Cretaceous period (Constenius, 1996; DeCelles, 2004; Dickinson, 2004). Lithospheric hydration further facilitated emplacement of the Idaho and Boulder batholiths (DeCelles, 2004; Yonkee and

Weil, 2015) and related Mesozoic volcanic activity, such as the Elkhorn Mountain volcanics (McDonald et al., 2020).
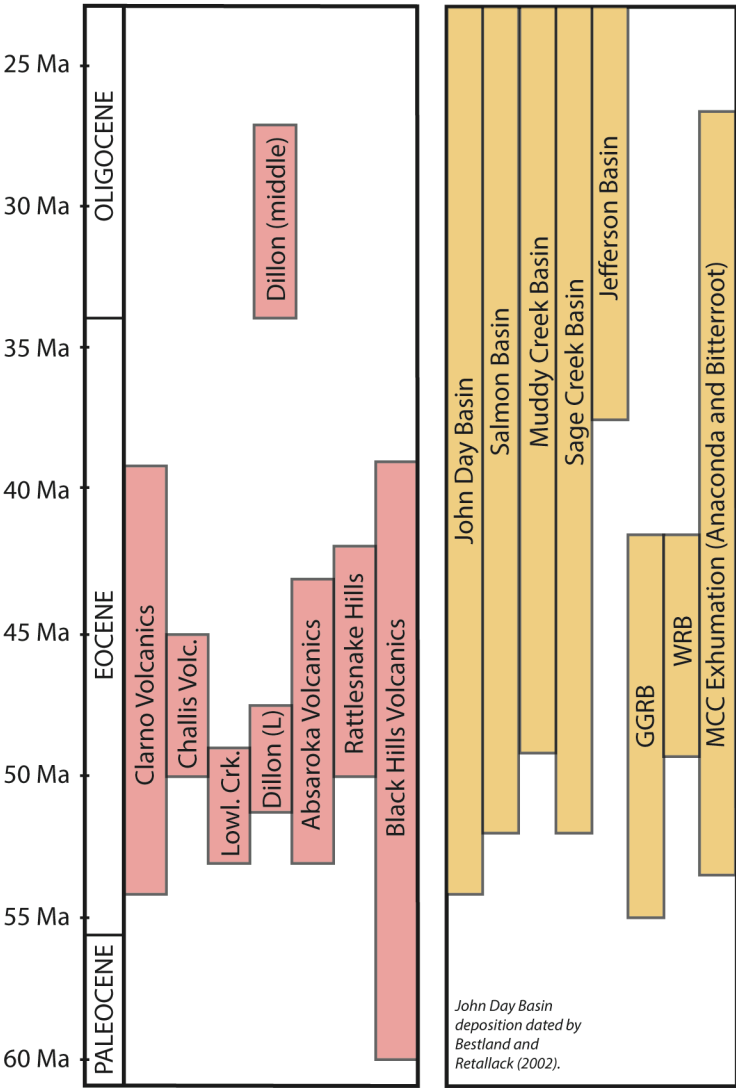
Figure 2.1. Chart comparing the ages of volcanic centers and depositional ages of strata within regional basins. After Smith et al. (2008) and Schwartz et al. (2019) and citations therein. GGRB = Greater Green River Basin; WRB = Wind River Basin.

The transition to flat-slab subduction in the Late Cretaceous initiated Laramide-style thick-skinned thrusting of basement-cored uplifts east of the Sevier thrust belt while occasionally overlapping in time and place with the location of Sevier-style compressional deformation (Humphreys, 2009). These uplifts partitioned the Sevier foreland, bounding a

system of internally drained basins beginning by 53 Ma (Fig. 2.1; Smith et al., 2008). Rapid basin subsidence, sedimentation from nearby uplifts and volcanic centers, and environmental conditions promoting preservation of carbonaceous material initiated the generation of key hydrocarbon reserves, such as the lacustrine Green River Formation (Smith et al., 2008; Chetel et al., 2011).

Western North America experienced a shift to an extensional tectonic regime associated with Farallon slab rollback in the Eocene (56-34 Ma). This is recorded in metamorphic core complex exhumation and extensional basin formation, resumed volcanism, and thermal uplift (Coney and Harms, 1984; Constenius, 1996; Smith et al., 2008; 2014; Chamberlain et al., 2012). Volcanic activity and subsequent thermal uplift to estimated elevations of 3.5-4 km began in British Columbia in the early Eocene and migrated southwestward into Nevada and Utah by the late Eocene – Oligocene (Mulch et al., 2007; Humphreys, 2009; 2015; Chamberlain et al., 2012; Smith et al., 2014; Cassel et al., 2014; 2018). While there is a recorded change in tectonomagmatic behavior from north to south related to slab rollback, effects of these changes on surface deformation are poorly constrained (Dickinson et al., 1988; Fan and Carrappa, 2014).

2.2. Eocene Volcanism

In the U.S. Cordillera, early to middle Eocene volcanic centers, including the Absaroka volcanic province (MT, WY) and the Challis volcanic field (ID), periodically blanketed the region in air-fall and ignimbrite deposits (Figs. 1.1; 1.2) (Smedes and Protska, 1972; M'Gonigle and Dalrymple, 1996; Hiza, 1999). Researchers assert that Farallon slab rollback and lithospheric delamination are largely responsible for the increased magmatism. The removal of the Farallon slab increased lower and mid-crustal heat flow and hydrated the overlying crust to lower the liquidus, initiating a southward-migrating ignimbrite flare-up in line with the location of the slab hinge (Coney and Harms, 1984; Sonder and Jones, 1999; Dickinson, 2004; Humphreys, 2009; Cassel et al., 2018).

2.2.1. Absaroka Volcanic Province

The Absaroka Supergroup (53-43 Ma) resulted from the most prolific Eocene volcanic field in the northern Rocky Mountains, erupting over 23,000 km^3 of volcanic

material over 25,000 km^2 (Smedes and Protska, 1972; Hiza, 1999; Harlan, 2006). Estimates of volumetric output place 60% of the Absaroka Supergroup as erupted from 49-47 Ma (Hiza, 1999). Examination of the more than 10 individual volcanic centers documents a northwest to southeast age progression based on $^{40}Ar/^{39}Ar$ age determinations (Hiza, 1999). Mafic volcanism occurred early in each volcanic center within the province, followed by volcanism characterized by an increased crustal melt component and higher silica content with time, though there is no discernible spatial trend across the entirety of the province (Hiza, 1999). Numerous sedimentary basins in Wyoming preserve Absaroka ash-fall deposits interbedded in lacustrine strata, including those of the Greater Green River, Wind River, and Bighorn Basins (Van Houten, 1964; Smith et al., 2008; Chetel et al., 2011).

2.2.2. Challis Volcanic Field

The Challis Volcanic Group of central Idaho (50-45 Ma; $^{40}Ar/^{39}Ar$) is the remnant of a short-lived but intense period of middle Eocene volcanism (Janecke and Snee, 1993; M'Gonigle and Dalrymple, 1996). The Challis Group is composed of andesitic lava flows, caldera-sourced ignimbrites, and a series of granitic intrusions and mafic dikes emplaced into the Cretaceous Idaho Batholith (Janecke and Snee, 1993; M'Gonigle and Dalrymple, 1996; Sanford, 2005). Effusive volcanism was mostly located in the southeastern portion of the field and spanned the earlier part of volcanic activity (~50-47 Ma), whereas more explosive silicic volcanism was largely concentrated along the central axis of the volcanic field between 48-45 Ma, exemplifying the bimodal nature of the sequence (Janecke and Snee, 1993; Sanford, 2005). The younger ash-falls and ignimbrites have a more uniform thickness and are more continuous than their earlier andesitic and dacitic counterparts. Multiple studies suggest this is the result of Challis effusive volcanism filling pre-volcanic paleotopography, followed by the broad distribution of volcaniclastic material unencumbered by topographic relief (Janecke and Snee, 1993; Janecke et al., 2000; Stroup, 2008). Challis volcaniclastic sediment is preserved in basins in southwestern Montana, eastern Idaho, and southwestern Wyoming (Janecke, 1994; M'Gonigle and Dalrymple, 1996; Chetel et al., 2011).

2.2.3. Lowland Creek Volcanics

The oldest Eocene volcanic center in Montana is documented in the west-central part of the state. The Lowland Creek volcanics, northwest of Butte, are characterized by two main ignimbrite sheets erupted between ~53-49 Ma, based on $^{40}Ar/^{39}Ar$ dating, overlapping in time with Absaroka volcanism and predating Challis volcanism by 3 Ma (Dudas et al., 2010; Scarberry et al., 2015; McDonald et al., 2020). Lowland Creek volcanism ranges from silicic to calc-alkaline andesitic in composition and is largely confined to west-central Montana (Dudas, 2010).

2.2.4. Dillon Volcanics

The bimodal Dillon volcanics of southwest Montana are marked by thin, discontinuous lava flows and rhyolitic tuffs, active from ca. 53 Ma-20 Ma (Fritz et al., 2007). Whole-rock K-Ar age determinations of the lower Dillon volcanics yield ages between ~49-42 Ma, making them largely contemporaneous with the Absaroka, Challis, and Clarno volcanic provinces (Fritz et al., 2007). The volumetrically smaller and less felsic middle Dillon volcanics were active from the latest Eocene to late Oligocene (34-27 Ma) and had an eruptive center near Virginia City (Fritz et al., 2007). Overall, the Dillon volcanics are spatially limited to the far western edge of southwest Montana.

2.2.5. Clarno Volcanic Province

The Clarno volcanic province was active from 54 – 39 Ma, based on $^{40}Ar/^{39}Ar$ ages, and erupted lavas and air-fall tuffs with compositions reflective of intermediate calc-alkaline arc volcanism (Bestland et al., 1999; 2002). Ca. 42 Ma, volcanic activity shifted to the Cascade arc and took on an intra-plate composition, depositing the air-fall tuffs and ignimbrites of the John Day Formation (Bestland et al., 2002). However, the timing of the formation of the Cascade Range is still debated (e.g., Kohn et al., 2002; Kukla et al., 2021). Early Cascade volcanism continued through the early Miocene (39-18 Ma; sanidine $^{40}Ar/^{39}Ar$ ages), resulting in a series of rhyolitic caldera-forming eruptions in eastern Oregon of mainly Oligocene age (McClaughry et al., 2009, 2010; Brown, 2017) and in more intermediate-mafic flows and tuffs of the Little Butte Volcanics to the west (Savoie, 2013; Ferreira, 2016).

2.2.6. Other Volcanic Centers

Igneous activity in the Black Hills, SD and the Devils Tower area, WY was the easternmost extent of Paleogene volcanic activity. Volcanism here was diverse in composition and activity lasted from ~60 Ma to 39 Ma, though most activity occurred between 58 and 50 Ma (Lisenbee, 1988; Redden and DeWitt, 2008). These units are predominantly alkalic iron-rich rocks, but compositions range from carbonatite to rhyolite (Lisenbee, 1988). To the west, the Rattlesnake Hills volcanic center of central WY was a small (~400 km^2) and short-lived (~50-42 Ma; K-Ar ages) volcanic center characterized by alkaline to subalkaline plugs, dikes, and flows (Sheriff and Shive, 1980; Wilson et al., 2016). Volcaniclastic material sourced from a Rattlesnake Hills quartz-latite eruption has been found in the nearby middle-late Eocene Wagon Bed Formation in the Beaver Rim area (Sheriff and Shive, 1980; Hausel, 1996).

3. METHODS

3.1. Geochemistry

Precipitation δD values respond to changes in elevation. As moist airmasses rise to pass over high topography, they adiabatically cool and rain out. Heavier mass isotopes preferentially condense out of vapor in equilibrium, leaving the remaining airmass depleted in D relative to its starting δD$_{vapor}$ value (Fig. 3.1; Dansgaard, 1964; Hoefs, 1997). Similarly, river waters draining areas of high elevation are generally D-depleted relative to downstream river waters, where drainage areas are larger and the hypsometric mean elevation is lower (Chamberlain and Poage, 2001; Kendall and Coplen, 2001; Rowley, 2007). This effect is seen especially well on the westward slope of the Cascade Range; δD$_{water}$ samples collected at high elevations are more negative than their low-elevation counterparts (Fig. 3.2). The modern lapse rate δD$_{water}$ is -21‰/1 km of elevation gain (Sharp, 2017).

Climate and atmospheric circulation patterns also play large roles in precipitation δD value patterns across continents. Warmer (cooler) temperatures reduce (increase) the δD$_{vapor}$ fractionation factor during initial evaporation resulting in airmass formation, leading to higher (lower) δD$_{vapor}$ vs. elevation lapse rates. (Dansgaard, 1964). Today, at mid- and high latitudes, a 1°C decrease in mean air temperature yields a 5.6‰ decrease in the δD$_{water}$ value (Rowley, 2001; Sharp, 2017). Similarly, relative humidity affects evaporation and

condensation of surface water and water vapor; low relative humidity generally enables increased evaporation, which preferentially results in D-enriched surface waters, and inhibits condensation, which conversely results in a more D-enriched airmass (Dansgaard, 1964).
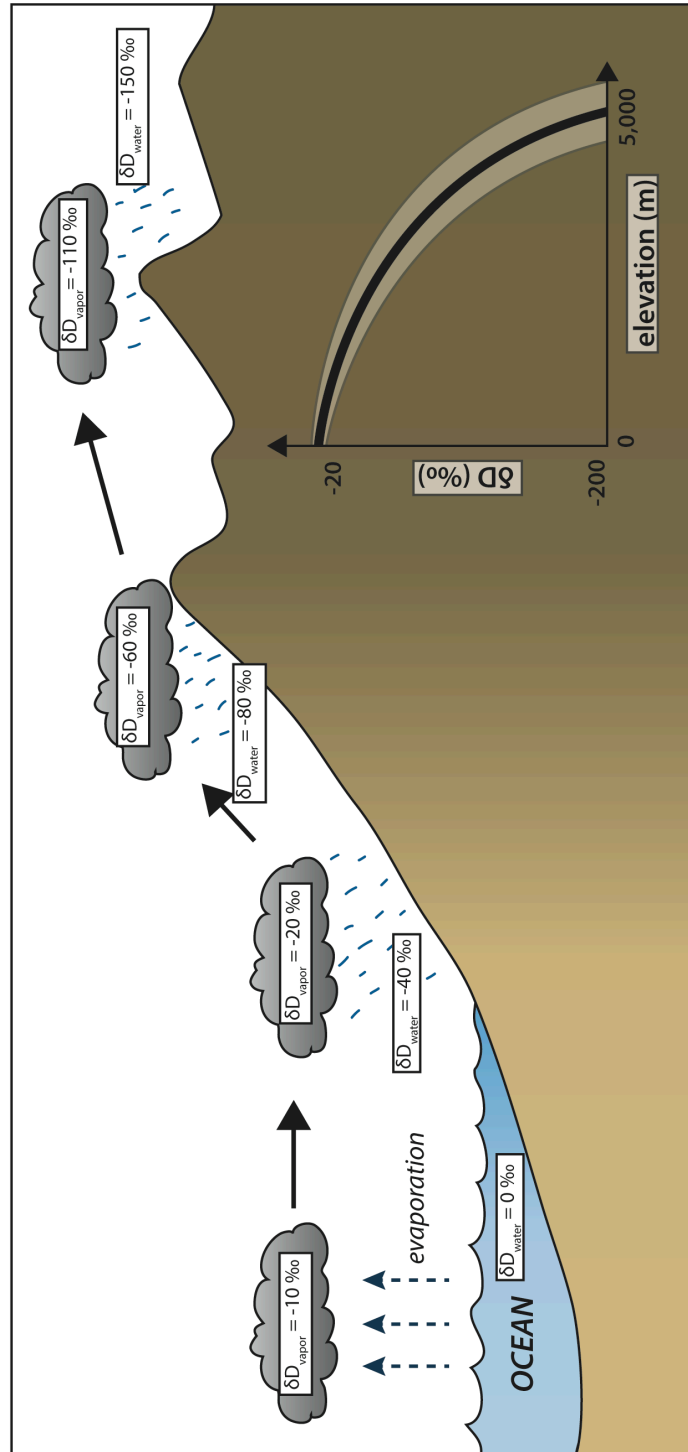
Figure 3.1. Schematic diagram of Rayleigh distillation. Adapted from Hoefs (1997).

An additional factor influencing the character and pattern of the modern isoscape is airmass trajectory over or around high topography (Galewsky, 2009; Vachon et al., 2010). Long mountain ranges oriented perpendicular to the direction of airmass travel, like the northern U.S. Cordillera, force airmasses to travel up and over topography, which is required to drive rainout (Galewsky, 2009). The shape, size, and geographical extent of a mountain range in the path of an airmass control the trajectory of the airmass and the climate patterns nearby, affecting regional ecological processes and weather patterns.
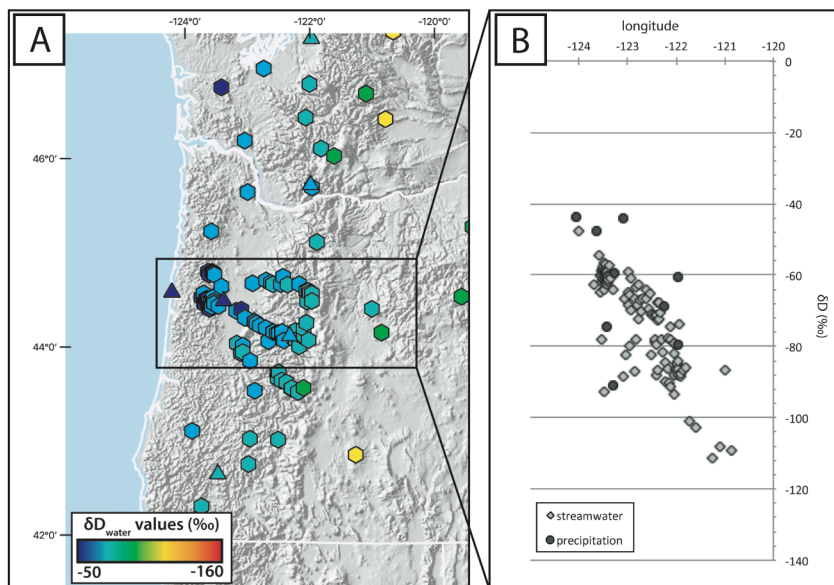
Figure 3.2. A) Map of modern stream δD_{water} values across the modern Cascade Range in Oregon. Triangles are small-catchment stream values from Bershaw et al., 2020. B) Transect from the windward side of the Cascades showing inverse relationship between longitude and δD_{water} values, attributed to elevation increase.

Felsic volcanic glass hydrates during contact with surface waters following deposition. Cation exchange of mobile elements, like Na^+, K^+, Ca^{2+}, and Mg^{2+}, for hydrogen ions creates a dense silicate "passivating layer," typically within ~10,000 years of eruption and deposition (Gin et al., 2013, 2015; Cassel and Breecker, 2017). Once formed, this nanoporous silicate rind prevents further contact or exchange with hydrating surface waters. This insulates the glass from the effects of changing hydration waters over time, preserving the water isotopic signature of the original depositional environment (Cassel and Breecker, 2017).

3.2. Sample Collection and Processing

3.2.1. Rocks

Samples were collected from ignimbrites and tuffaceous deposits like tuffaceous sandstone, siltstone, and airfall tuff. Locations were chosen based on accessibility and strategic location within study area. All potentially viable samples in a locality were collected, but sample beds with little to no reworking and minimal alteration were placed at a higher priority than moderately to heavily reworked or altered deposits. Minimal reworking is an indicator of hydration by precipitation water as opposed to material reworked and hydrated by lake or river water, so those samples provide the δD values closest to original precipitation (Cassel et al., 2018). Unwelded ignimbrite deposits were preferred over welded deposits because surface waters can more easily infiltrate the rock at the time of deposition (Cassel and Breecker, 2017).

Following the methods of Cassel and Breecker (2017), glass-bearing samples were separated to >95% pure glass prior to analysis. Samples were crushed with a ceramic mortar and pestle or a disc mill fitted with ceramic milling plates. Crushed samples were wet-sieved through nylon sieve cloth at 150, 70, and 37 μm. Glass was most abundant in the 70>150 and 37>70 μm fractions. The >150 μm size fraction typically exhibited a greater degree of alteration, and the <37 μm size fraction contained mostly clay particles. Acid abrasion with hydrochloric acid (HCl) and hydrofluoric acid (HF) removed carbonate material and broke down clay minerals to avoid compromising glass purity with other crystalline components. Samples were rinsed twice for 30 seconds in 10% HCl and twice for 30 seconds in 8% HF, each followed by a rinse with 18 mΩ deionized water. Any samples with remaining clay

components underwent up to two additional HF abrasions. Following treatments, samples were thoroughly rinsed and re-seived to 70>150 and 37>70 μm. A neodymium hand magnet, followed by runs through a Frantz isodynamic separator at 0.3 and 0.8 amps, removed magnetic minerals. Samples were then separated by density using lithium metatungstate (LMT) or methylene iodide (MEI) to >95% glass purity. Solutions started at ρ=2.7 g/mL before additional dilution and stratification in a modified 500 mL separation funnel. Following separation, samples were rinsed thoroughly and ultrasonicated with 18 mΩ deionized water or acetone to remove residual LMT or MEI (Fig. 3.3).

3.2.2. Modern Waters

Small-catchment stream water samples were collected to provide an estimate of local precipitation δD values and to expand the current water stable isotopic dataset (e.g., Bershaw et al., 2020). 45 samples were taken in 20 mL glass headspace vials with PTFE lined caps. Water temperature was measured at time of collection using a thermocouple temperature probe. Care was taken to avoid irrigation waters, which may not accurately represent local precipitation δD and $\delta^{18}O$ values due to recycled water supplies (Kendall and Coplen, 2001). After collection, sample vials were hand-tightened and sealed with Parafilm and electrical tape to prevent leakage or isotopic exchange with the atmosphere.

The modern water dataset used in this study also includes δD and $\delta^{18}O$ values from 697 stream samples and 66 precipitation samples taken over the past 35 years from the Waterisotopes Database (2020), the **U**nited **S**tates **N**etwork for **I**sotopes in **P**recipitation (USNIP), and the **G**lobal **N**etwork for **I**sotopes in **P**recipitation (GNIP) (IAEA/WMO, 2021). Samples were selected from small creeks or streams close to the headwaters to more closely reflect precipitation values. Stream values were averaged summer (May – September) values at each site to remain consistent with the summer field sampling timeframe for this study. Precipitation samples are winter values (October – April), which contribute most heavily to summer streamwater and melt values in the study region (Vachon et al., 2007).
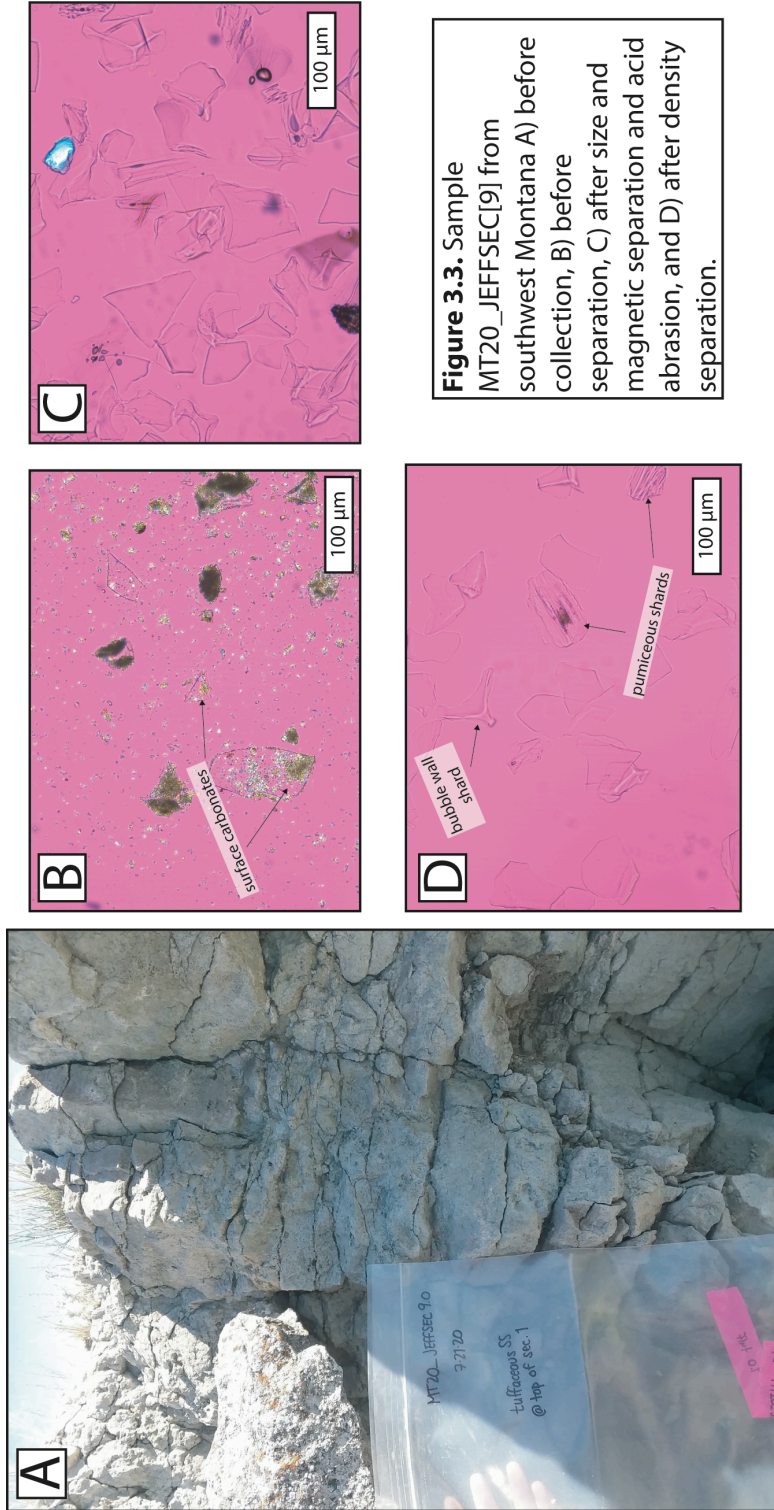
Figure 3.3. Sample MT20_JEFFSEC[9] from southwest Montana A) before collection, B) before separation, C) after size and magnetic separation and acid abrasion, and D) after density separation.

3.3. Sample Analysis

3.3.1. Stable Isotopes

Glass samples were analyzed for hydrogen stable isotope ratios at the Barnes-Breecker Light Stable Isotope Lab at the University of Texas – Austin. Glass δD values from 37 new samples were measured by high temperature thermal combustion (1450°C) and continuous-flow gas mass spectrometry on a Thermo Electron TC-EA coupled to a Thermo MAT253 isotope ratio mass spectrometer (IRMS). Following the sample preparation protocols outlined by Cassel and Breecker (2017), three to six aliquots of 3.0-3.3 mg of pure glass shards were placed in 3.5 – 5 mm Costech silver foil capsules, dried under a vacuum at 70°C for 12-24 hours, and then loaded into a zero-blank auto sampler and immediately flushed with dry He gas. Unknowns were run interspersed with internationally certified standards USGS-57 (biotite; -91.5‰), USGS-58 (muscovite; -28.4‰), and NBS-22 (oil; -119.6‰) and an in-house glass standard (-163‰). Resultant δD_{glass} values were corrected for instrumental drift, peak amplitude, and normalized to the VSMOW scale. Aliquots with significant memory effects (>5‰) were eliminated from sample means. Each sample mean represents an average of 2-6 aliquots. δD value precision was determined to be 2.4‰ (2σ of replicate standards). Water contents were calculated from total H and mass for each aliquot and reported in wt. percent.

Stream water samples were also analyzed at UT-Austin for both δD and $\delta^{18}O$ values. δD values were obtained via the TC-EA/MAT253 IRMS as with the glass samples. $\delta^{18}O$ values were delivered via a GasBench system operated in continuous flow mode. As with glass analysis, water samples were run against international standards and in-house working standards and corrected for instrument drift, peak amplitude, and normalized to the VSMOW scale.

3.3.2. Trace and Rare Earth Elements

To distinguish volcanic sources, trace and rare earth element (TREE) concentrations for 29 volcanic glass samples were analyzed at the Washington State University Peter Hooper Geoanalytical Lab. For each sample, 0.10-0.50 g of material were prepared for mass spectrometry with a straight dissolution technique using 69-70% HNO_3, 48-52% HF, 67-71% $HClO_4$, and H_2O_2. Samples were then run on an Agilent 7700 inductively coupled plasma

mass spectrometer (ICP-MS). Processing of three in-house rock standards ensured standardization, and elemental concentrations, oxide corrections, and drift corrections were performed following analysis. Long-term precision is reported as <5% for rare earth elements and <10% for trace elements.

3.4. Paleoelevation Model

Paleoelevation estimates from δD_{glass} values were calculated using the one-dimensional thermodynamic airmass lifting Rayleigh distillation ("rainout") model of Rowley et al. (2001; later modified in Rowley, 2007; Rowley and Garzione, 2007). Changes in air temperature due to climate and elevation are reflected in the model's temperature-dependent vapor-liquid fractionation factor (Rowley et al., 2001). A single airmass trajectory is considered from the west coast (Vachon et al., 2010). The model incorporates estimates of initial temperature, initial relative humidity (RH), air pressure at the lifting condensation level, and local meteoric water line (LMWL) equations to calculate elevation estimates based on the change in δD_{glass} values ($\Delta \delta D$).

Secular changes in the δD value of the vapor source are controlled for by comparing all δD values to a low-elevation datum. In this case, glass $\Delta \delta D$ values were calculated using a near-sea level sample in western Oregon. This determination was based on the local stratigraphy and previous $^{40}Ar/^{39}Ar$ age dating of glass-bearing units. The OR21_506WV unit, dated at 26.28 ± 0.18 Ma (Table 3.1) overlies the marine facies of the Eocene-Oligocene Eugene Formation, confirming the likely low elevation of this sample during deposition and hydration (Retallack et al., 2004; McClaughry et al., 2009). The Eugene Formation and other contemporaneous marine facies are thickest in the Oregon Coast Range (>5 km thick) and thin to <1 km beneath the Little Butte Volcanics and Cascade Range, indicating that the Eocene paleoshoreline was located approximately 100 km inland of the modern shoreline and likely within a few kilometers of OR21_506WV (McClaughry, 2010).

To calibrate the rainout model, modern small-catchment stream water sample δD values (Bershaw et al., 2020; Waterisotopes Databases, 2020) and modern climate parameters were used and elevation estimates were compared to modern elevations (Table 3.2; Fig. 3.4). The modern mean annual temperature (MAT), altitude where precipitation occurs, and average relative humidity (RH) during precipitation events at the ~45°N latitude

Table 3.1. Volcanic glass sample results listed by sample age.

Sample No.	Latitude N	Longitude W	δD value (‰)	2σ	Water content (%)	Age (Ma)	Dating Method	Age Citation
ND20_404SB A	47.641	-103.368	-177.1	0.65	7.59	58	MDA	Li & Fan, 2018
ND20_404SB B	47.641	-103.368	-171.6	0.70	8.00	58	MDA	Li & Fan, 2018
ND20_402SB A	47.647	-103.336	-163.0	1.78	7.83	58	MDA	Li & Fan, 2018
18MT_129CR	46.019	-112.749	-186.0	1.27	3.82	53.1	bt $^{40}Ar/^{39}Ar$	Dudas, 2010
18MT_108 Liva Ln - A	46.045	-112.620	-201.8	1.19	6.04	53.1	bt $^{40}Ar/^{39}Ar$	Dudas, 2010
18MT_117GRA*	45.056	-110.779	-98.4	2.17	10.33	53	bt $^{40}Ar/^{39}Ar$	Hiza, 2000
18MT_112VCB	45.299	-111.931	-190.7	2.17	6.55	49.3, 52	bt, plag K/Ar	Marvin et al., 1974
WU14-052WR B	42.872	-108.311	-117.1	3.64	9.93	51.74	sanidine $^{40}Ar/^{39}Ar$	Smith et al., 2008
WY19_345CP-B	42.268	-108.717	-127.8	0.14	6.07	48.89	single grain $^{206}U/^{238}Pb$	Tsukui, 2016
WU14_SCM-1	41.132	-110.137	-170.2	2.40	5.84	47.45	sanidine $^{40}Ar/^{39}Ar$	Smith et al., 2008
WU14-048MC-A*	44.737	-112.895	-99.9	3.78	10.26	47.07	sanidine $^{40}Ar/^{39}Ar$	M'Gonigle & Dalrymple, 1996
WY20_444WB A*	43.579	-107.614	-108.7	3.46	10.72	~46.2	NALMA	VanHouten, 1964
WY20_452WB A	42.722	-108.173	-174.4	0.72	5.79	~46.2	NALMA	VanHouten, 1964
WY20_451WB A	42.723	-108.170	-173.5	1.08	5.63	~46.2	NALMA	VanHouten, 1964
WY20_450WB A	42.724	-108.169	-162.6	2.48	6.12	~46.2	NALMA	VanHouten, 1964
18MT_113GLEN - B	45.127	-112.750	-157.5	1.26	7.84	46.1	plag K/Ar	Smedes & Herman, 1965
WY19_338AB-B	43.734	-109.979	-97.1	1.82	8.66	44-47	sanidine $^{40}Ar/^{39}Ar$, map correlation	Smedes & Protska, 1972
18WY_123SLT-D*	43.778	-109.021	-113.5	3.16	11.09	44-47	sanidine $^{40}Ar/^{39}Ar$, map correlation	Smedes & Protska, 1972
18MT_114SCB	44.771	-112.597	-172.9	0.64	6.31	45.54	sanidine $^{40}Ar/^{39}Ar$	M'Gonigle & Dalrymple, 1996
MT15_016CC	44.634	-112.966	-164.4	1.40	5.48	43-47	sanidine $^{40}Ar/^{39}Ar$, map correlation	Janecke & Snee, 1993; M'Gonigle & Dalrymple, 1996
MT20_464MC	44.714	-112.911	-136.0	1.11	1.28	43-47	sanidine $^{40}Ar/^{39}Ar$, map correlation	Janecke & Snee, 1993; M'Gonigle & Dalrymple, 1996
MT20_465MC A	44.725	-112.892	-116.9	0.46	8.21	43-47	sanidine $^{40}Ar/^{39}Ar$, map correlation	Janecke & Snee, 1993; M'Gonigle & Dalrymple, 1996
MT15-008SC	44.872	-112.760	-157.2	1.30	7.34	43-47	sanidine $^{40}Ar/^{39}Ar$, map correlation	M'Gonigle & Dalrymple, 1996
18ID_104PC	42.749	-116.309	-119.3	2.56	0.61	43-47	map correlation	Hansen & Pearsen, 2016
16OR_003JD	44.637	-120.221	-103.8	4.14	6.80	39.2	sanidine $^{40}Ar/^{39}Ar$	Bestland & Retallack, 1994
WU14_012ML	39.575	-113.051	-136.6	1.18	3.51	~35	sanidine $^{40}Ar/^{39}Ar$, map correlation	Cassel et al., 2018
MT20_JEFFSEC[0]	45.796	-111.472	-183.7	0.62	5.44	33-37	NALMA	Tabrum et al., 2001; Vuke, 2003
MT19_344TF-A	45.797	-111.472	-182.4	0.80	6.30	33-37	NALMA	Tabrum et al., 2001; Vuke, 2003
MT20_JEFFSEC[9]	45.797	-111.472	-179.5	3.68	5.31	33-37	NALMA	Tabrum et al., 2001; Vuke, 2003
SD20_406BL*	45.372	-103.159	-88.9	2.24	10.37	32?	map correlation	Fahrenbach & Sawyer, 2011
MT20_424CF B	46.644	-111.879	-188.9	1.12	5.23	<35	map correlation	Vuke, 2011
MT20_426CF A	46.764	-111.771	-189.4	1.88	7.40	<35	map correlation	Vuke, 2011
MT20_426CF B	46.764	-111.771	-177.8	3.28	7.83	<35	map correlation	Vuke, 2011
UT15_033DP	40.648	-109.301	-163.6	1.76	5.42	29.5 ± 1.08	bt K/Ar	Marvin et al., 1970
OR21_505WV*	44.420	-122.666	-101.8	2.65	10.87	26.28	plag $^{40}Ar/^{39}Ar$	McClaughry et al., 2009
OR21_506WV*	44.420	-122.666	-96.0	3.76	10.91	26.28	plag $^{40}Ar/^{39}Ar$	McClaughry et al., 2009
MT20_476CF B	46.488	-111.532	-222.9	1.92	4.80	<23	map correlation	Vuke, 2011

Standard 2σ error is ± 2.4‰

* high water content

coastal region were determined by comparing these records with records of precipitation flux (Acker and Leptoukh, 2007; Thoning et al., 2021). The modern MAT of this area is ~9°C ± 2°C at 750 hPa (the pressure of the approximate lifting condensation level), and modern RH estimates range from 72% - 92% (Acker and Leptoukh, 2007). Based on modern stream water isotopic ratios from Bershaw et al. (2020), the modern Cascades LMWL is represented by the equation:

$$\delta D = \delta^{18}O(8.86) + 13.53$$

A representative model-observed fit indicates that the model can effectively predict elevations given δD_{water} values and climate parameters for regions where precipitation is dominated by a single source (Fig. 3.4).

Estimates of Paleogene terrestrial surface air temperature and RH were obtained from coastal paleofloral studies and paleoclimate models of the Pacific Northwest region (Retallack, 2004; Dunn, 2007; Yang et al., 2011; Feng et al., 2013; Anagnostou et al., 2016; Feng and Pouslen, 2016; Huber and Caballero, 2016; Zhu et al., 2019). **C**limate **L**eaf **A**nalysis **M**ultivariate **P**rogram (CLAMP) paleofloral parameters, climate models, and leaf margin analysis studies were all considered for estimates of Eocene – Oligocene air temperatures and RH (Table 3.2). Temperature estimates were generally in agreement across the studies (Huber and Caballero, 2011; Poulsen and Jeffery, 2011; Yang et al., 2011; Anagnostou et al., 2016). Paleoclimate studies estimate early Eocene global MATs to be up to 14°C warmer than modern temperatures, partially due to the high pCO$_2$ – two-to-five-times greater than modern (Thoning et al., 2021), though the warming effects of higher pCO$_2$

Table 3.2. Ranges of temperature estimates used in the paleoelevation model for each time slice.

Time slice (Ma)	Initial temperature anomaly range (above modern)	Method	Citation
58-50	7-12°C	pCO$_2$ - enabled modeling	Poulsen & Jeffrey, 2011; Huber & Caballero, 2011; Anagnostou et al., 2016; Zhu et al., 2019
49-43	6-10°C	CLAMP	Yang et al., 2011
42-35	4-8°C	leaf margin analysis, pCO$_2$-enabled modeling	Dilhoff et al., 2009; Anagnostou et al., 2016
35-21	0-4°C	leaf margin analysis, pCO$_2$-enabled modeling	Dilhoff et al., 2009; Yang et al., 2011

CLAMP: Climate Leaf Analysis Multivariate Program
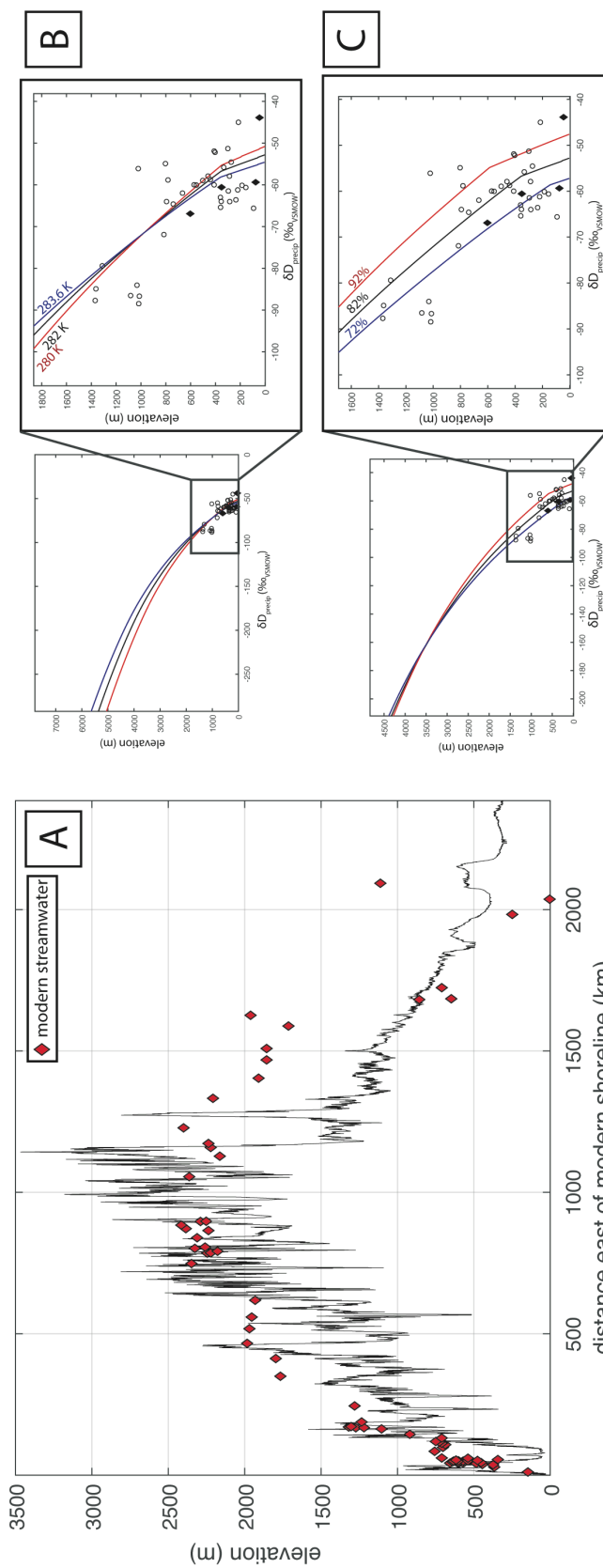
Figure 3.4. A) Plot of modeled elevations from modern stream waters, given the Cascades meteoric water line and a Pacific coast low-elevation datum of -6.76‰ of Bershaw et al. (2020). B) Cascades elevation calibration curve based on initial temperature estimates. The 282 K predictive line was found to be a good average for the data points and is used as the modern condensation temperature over coastal Oregon. Initial temperature was found to be more influential to paleoelevation estimates at elevations >2,500 m. C) Cascades elevation calibration curve based on estimates of initial relative humidity. 82% was found to fit the stream data well enough to use in the 1D predictive model. Note: relative humidity estimates are more influential at high elevation (<2,500 m) and has negligible influence beyond this cutoff.

were not as pronounced at higher latitudes in the Eocene as they are today (Poulsen and Jeffery, 2011; Anagnostou et al., 2016; Zhu et al., 2019). Paleogene shoreline paleotemperature ranges for each age category incorporated an error of ± 1-2°C (Table 3.2). Late Paleocene MATs are estimated at late Eocene temperatures (Zachos et al., 1994). A stepwise decrease in MAT over the course of the Eocene and into the Oligocene accounts for the overall cooling trend through the Eocene (Anagnostou et al., 2016). Eocene RH was set at 92%, the maximum modern RH during precipitation events; this is greater than the 75% estimated by Yang et al. (2011), but is likely to better reflect RH conditions during precipitation events and has negligible effects on paleoelevation estimates (<5‰ change in δD predicted value) or the modern calibration curves (Fig. 3.4). The model incorporates the analytical uncertainty of δD values into its error calculations, but uncertainty in initial temperature is the largest source of error. The high temperatures of the early Eocene have the greatest uncertainty due to a large temperature estimate range and high pCO_2.

4. RESULTS

4.1. Modern Waters δD and δ^{18}O Results

Modern stream and precipitation δD values range from -36‰ to -146‰ and -44‰ to -160‰, respectively. D-excess values range from -20‰ to 15‰. Samples collected as part of this study have δD values of -70‰ to -145‰ and d-excess values of -9‰ to 9‰, with one d-excess outlier of -27‰. In general, the most D-depleted samples measured were collected in southwestern and central Montana along the Sevier thrust front (Table 4.1). The data show that δD values decrease steadily from the Pacific coast until reaching central/southwest Montana, and then increase incrementally again across the Great Plains (Fig. 4.1). Additional data manipulations and charts are found in the appendix.

4.1.1. Cascade Range

Meteoric water δD values on the windward side of the Cascade Range (west of 121°W longitude) are D-enriched relative to the rest of the modern dataset (Figs. 3.2; 4.1). δD$_{water}$ values range from -41‰ along the Pacific Coast to -102‰ in the mountains. Stream

Table 4.1. Modern small-stream sample $\delta^{18}O$ and δD results from this study.

Sample No.	Latitude	Longitude	Elevation (m)	Water Temp (°C)	$\delta^{18}O$ (‰)	δD (‰)	d-excess (‰)
MT20_R44	46.776	-114.384	1144	16.4	-16.7	-126.5	7.4
MT19-R07	46.574	-114.135	1110	12.3	-16.3	-134.3	-3.9
MT19-R06	46.625	-114.104	1045	23.4	-16.7	-127.8	6.1
MT19-R04	46.597	-114.024	1086	17.1	-17.4	-132.6	6.4
MT20_R47	48.334	-114.015	1193	11.3	-16.3	-123.5	7.1
ID20_R30	45.655	-113.973	1741	6.8	-17.5	-132.3	7.6
MT19-R05	46.646	-113.963	1155	10.7	-16.8	-135.9	-1.9
ID20_R32	45.098	-113.954	1431	8.9	-17.6	-135.7	5.4
ID20_R31	45.200	-113.931	1358	13.6	-16.7	-134.6	-1.3
MT20_R46	48.185	-113.922	1713	7.2	-15.8	-117.2	9.0
ID19-R08	45.089	-113.880	1366	13.5	-17.5	-131.8	8.1
MT20_R45	45.656	-113.796	1943	15.6	-17.4	-133.4	5.8
ID19-R09	44.522	-113.710	1816	9.6	-16.8	-137.4	-3.4
ID20_R33	45.005	-113.701	1546	7.3	-17.8	-136.9	5.4
ID19-R10	44.273	-113.656	2082	10.3	-18.1	-139.5	5.5
MT20_R26	46.235	-113.289	1759	5.4	-17.1	-134.2	2.9
MT20_R25	44.849	-113.284	2121	13.8	-18.0	-139.9	4.4
MT20_R27	46.489	-113.143	1685	-	-17.1	-133.0	4.1
MT20_R34	46.147	-113.143	1965	6.7	-17.8	-138.3	4.1
MT20_R24	46.142	-113.127	1978	6	-17.2	-131.9	5.5
MT20_R23	46.177	-113.053	1899	6.4	-17.6	-136.4	4.6
MT19-R02	45.993	-113.035	1961	12	-18.3	-141.7	4.7
MT20_R42	44.714	-112.910	2444	9.5	-18.5	-144.6	3.1
MT19-R03	46.254	-112.901	1645	7.9	-18.4	-140.7	6.5
MT20_R41	44.581	-112.679	2036	7.3	-17.9	-138.5	4.8
MT20_R40	44.572	-112.672	2078	7.2	-17.7	-136.2	5.2
MT20_R43	46.887	-112.361	1437	13.8	-17.8	-135.8	6.6
MT19-R01	45.812	-112.114	1342	14.1	-17.1	-136.0	1.1
MT20_R28	46.709	-111.784	1153	16.3	-18.5	-144.5	3.9
WY19-R18	45.963	-111.182	1425	19.1	-18.2	-142.2	3.2
MT20_R29	45.765	-110.988	1670	6.6	-17.8	-136.5	6.2
WY19-R12	43.760	-109.996	2795	4.8	-18.7	-142.0	7.6
WY19-R13	46.733	-109.978	2691	18.2	-18.5	-144.4	3.7
WY19-R14	43.721	-109.973	2616	13.9	-18.4	-140.9	6.2
WY19-R17	44.305	-109.275	2506	-	-17.5	-136.6	3.5
WY19-R16	44.299	-109.256	2603	22.1	-16.7	-129.8	4.0
WY20_R39	42.695	-108.907	2680	5.3	-18.0	-137.2	6.6
WY19-R15	43.693	-108.877	1996	22.4	-17.0	-134.6	1.6
MT20_R35	45.787	-108.857	1077	17.6	-13.8	-119.0	-8.7
WY20_R37	44.149	-107.250	2360	13.4	-17.1	-133.0	3.6
WY20_R38	44.234	-107.232	2667	6.4	-18.1	-139.7	4.8
WY20_R36	44.259	-107.212	2783	14.5	-17.4	-131.5	7.7
MT20_R20	47.640	-104.251	669	21.7	-15.7	-128.4	-2.5
SD20_R22	45.504	-103.319	879	21.9	-5.4	-69.6	-26.7
SD20_R21	45.410	-103.195	1014	22	-15.0	-119.5	0.3

and precipitation samples taken the farthest west have δD values between -50‰ and -65‰ (Fig. 4.1). Samples taken in the Cascades, close to -121°W, have more negative δD values between -70‰ and -95‰ (Fig. 3.2). D-excess values are generally positive in this zone, averaging 10‰ to 12‰ across the entirety of the longitudinal zone (Fig. 4.1).

4.1.2. West of the Sevier Thrust Front

Modern δD_{water} values between the Cascades and the eastern Rocky Mountain front (121°W – 109°W) decrease from west to east (Fig. 4.1). Highest δD values approach -100‰ and are most often found just east of the Cascades. The lowest δD_{water} values, -140‰ to -150‰ are found between 113°W and 110°W, which is the location of the highest mean topography. Inland of the Cascades but west of the Cordilleran thrust belt, sample δD_{water} values decrease gradually from -100‰ to -130‰ over 7° of longitude (121°W to 114°W). From 114°W to 113°W, though, δD_{water} values decrease from -130‰ to -150‰, then stay consistent until 110°W, when minimum δD_{waer} values increase slightly to -135‰. D-excess values in this region are generally positive, but slightly lower than along the Pacific coast, with an average of 8‰ west of 110°W. East of this point, d-excess values drop to an average of 6‰.

4.1.3. East of the Sevier Thrust Front

East of the Sevier thrust front, δD_{water} values increase incrementally from -145‰ in the western Great Plains to values that average close to -50‰ in the Midwest (Fig. 4.1). Most of this decrease, from -135‰ to -50‰, in observed between 105°W and 95°W. East of 95°W, δD_{water} values from precipitation decrease slightly to -65‰. Overall, d-excess values are lowest in this longitudinal zone with an average value of -1‰, but there is a great deal of d-excess variation in this region, with values as low as -19‰ (Fig. 4.1).

4.2. Glass δD Results

Samples range in age from late Oligocene to late Paleocene, with most samples taken from the early to middle Eocene (Table 3.1). Glass δD values range from -223.6‰ ± 0.1‰ to

-79‰ ± 6.9‰ (Table 3.1). The most D-depleted values are located in southwestern and central Montana, and the most D-enriched values are found in western Oregon (Fig. 4.2).
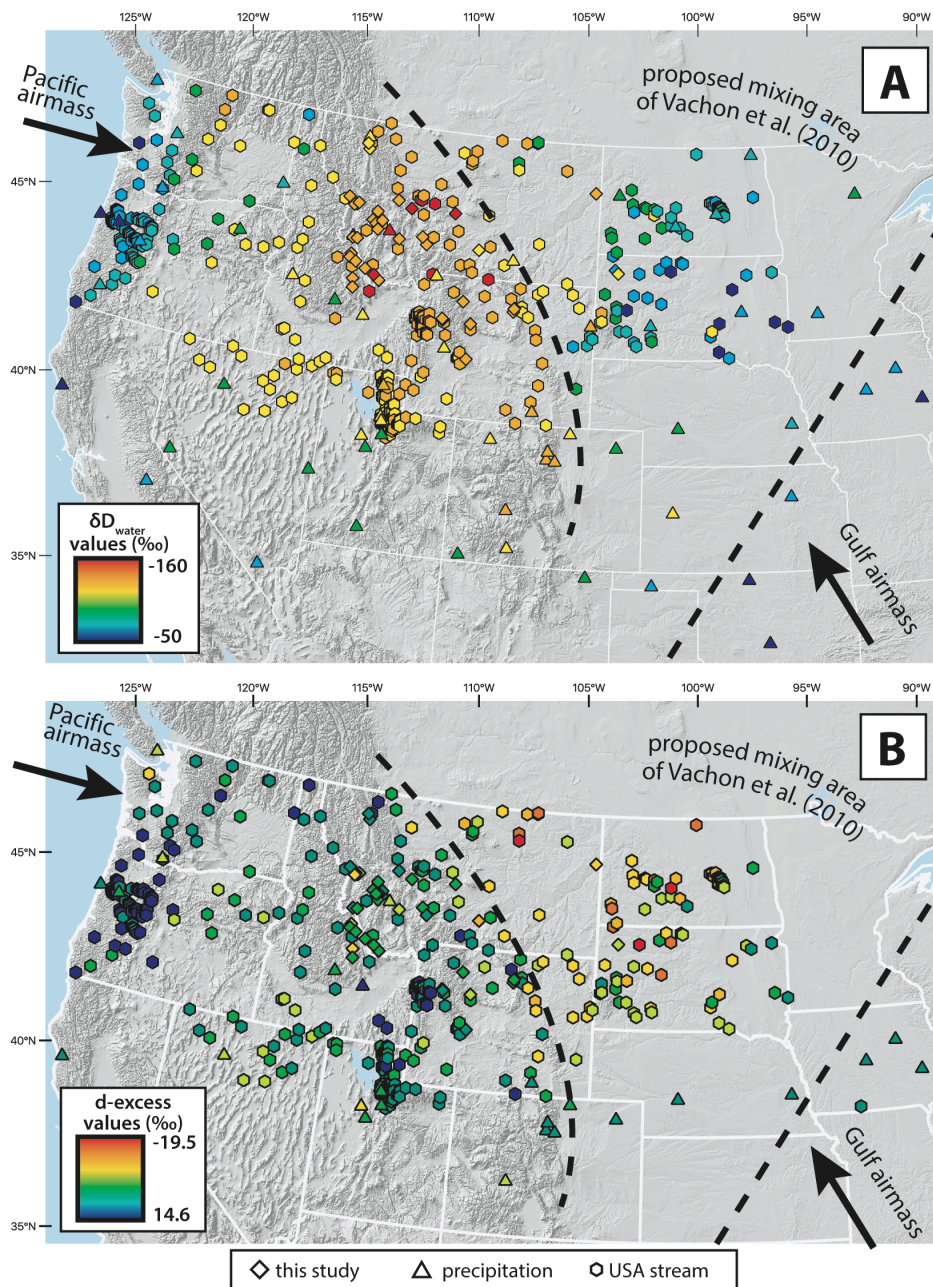
Figure 4.1. A) Map of modern winter precipitation and summer small-stream δD values from this study and USNIP, GNIP, and Wateristotopes databases. Precipitation data collected over > 1 years and averaged by season (winter: October - April; summer: May - September). B) Map of modern winter precipitation d-excess values. A distinct change to more negative d-excess values indicates airmass mixing or evaporation east of the Sevier fold-thrust belt in MT and east of the Laramide uplifts in WY. Arrows indicate direction of airmass travel.

In Oregon, three δD_{glass} values from this study range from -79‰ ± 9.6‰ to -103.8‰ ± 4.1‰, generally decreasing from west (124°W) to east (121°W) (Fig. 4.2). In Montana, δD values range from -95‰ ± 1.8‰ in the Muddy Creek basin in the southwest part of the state to -224‰ ± 0.1‰ in the west-central part of the state. In general, δD_{glass} values also decrease from west to east on the windward (west) side of the Rockies (Fig. 4.3). East of the Sevier thrust front, samples are highly variable and do not follow a specific pattern. δD_{glass} values during Eocene and Oligocene time span a δD range of nearly 100‰, from -89‰ ± 2.2‰ in early Oligocene South Dakota to -174‰ ± 0.7‰ in the Eocene Wind River Basin of Wyoming. Three Paleocene samples from North Dakota (ND20_402SB, ND20_404SB-A,B) have δD values ranging from -164‰ ± 0.9‰ to -177‰ ± 0.2‰ (Fig. 4.2).

Figure 4.2. Sample maps colored to reflect δD values. Maps are arranged by time: A) 58-50 Ma; B) 49-43 Ma; C) 42-35 Ma; D) 35-21 Ma. Sevier fold-thrust belt and major basins included. See legend for color scale and symbology.
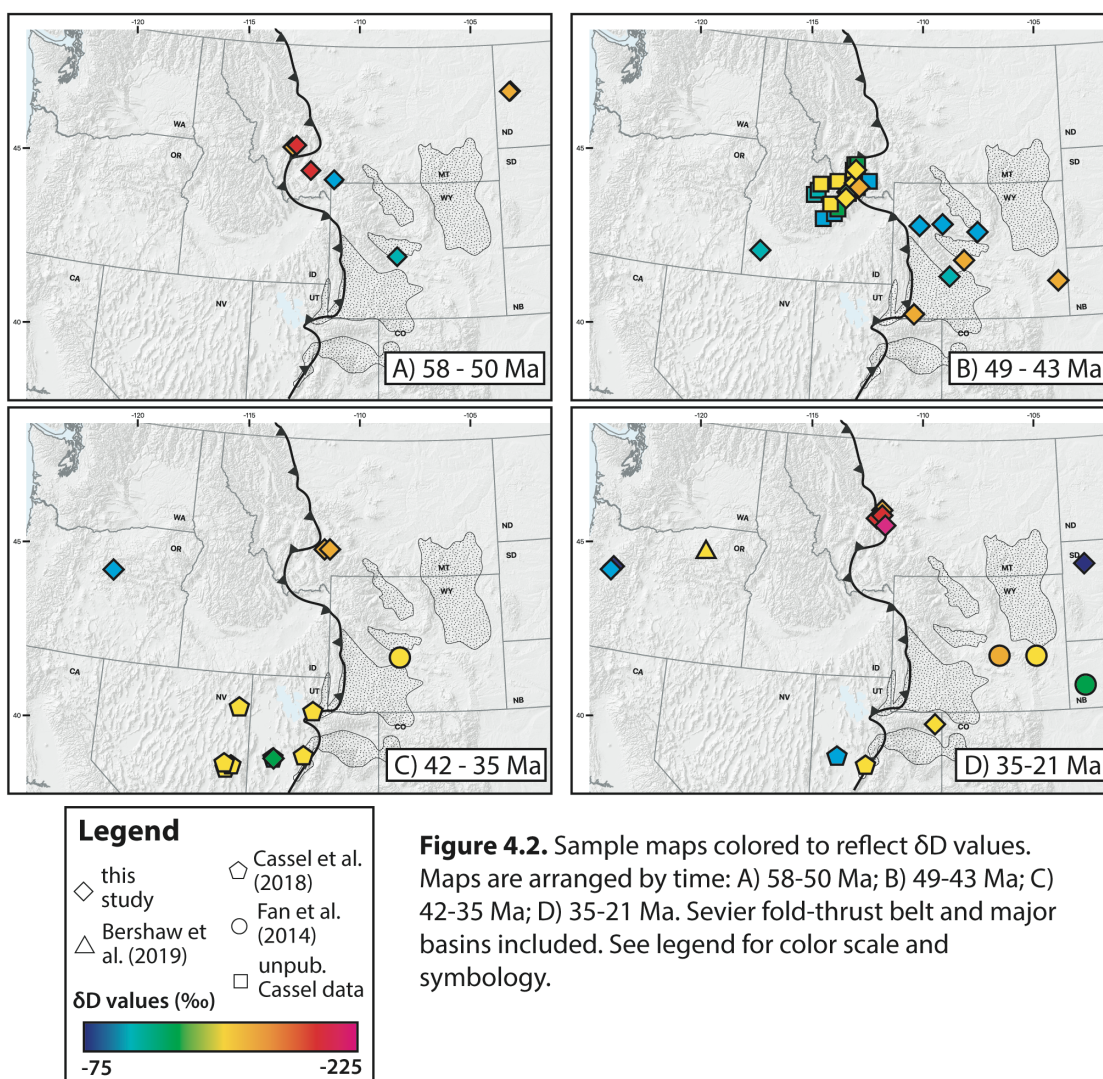
4.3. Trace and Rare Earth Element Concentrations

TREE elemental concentrations were normalized to chondrite values from McDonough and Sun (1995) and plotted in TREE spider diagrams (Fig. 4.4) and key TREE elemental fractionation diagrams (Fig. 4.5). Five groupings were identified based on comparisons among samples' light rare earth element (LREE) and heavy rare earth element (HREE) relative concentrations, similarities in immobile element concentration, including Zr, Th, Y, Yb, Hf, and the size and direction of europium anomalies (Eu/Eu*) (Hildreth and Mahood, 1985). Key patterns are summarized in Table 4.2.

Legend

δD values (‰)
-225 ◇ this study
△ Bershaw et al. (2019)
□ unpub. Cassel data
-75
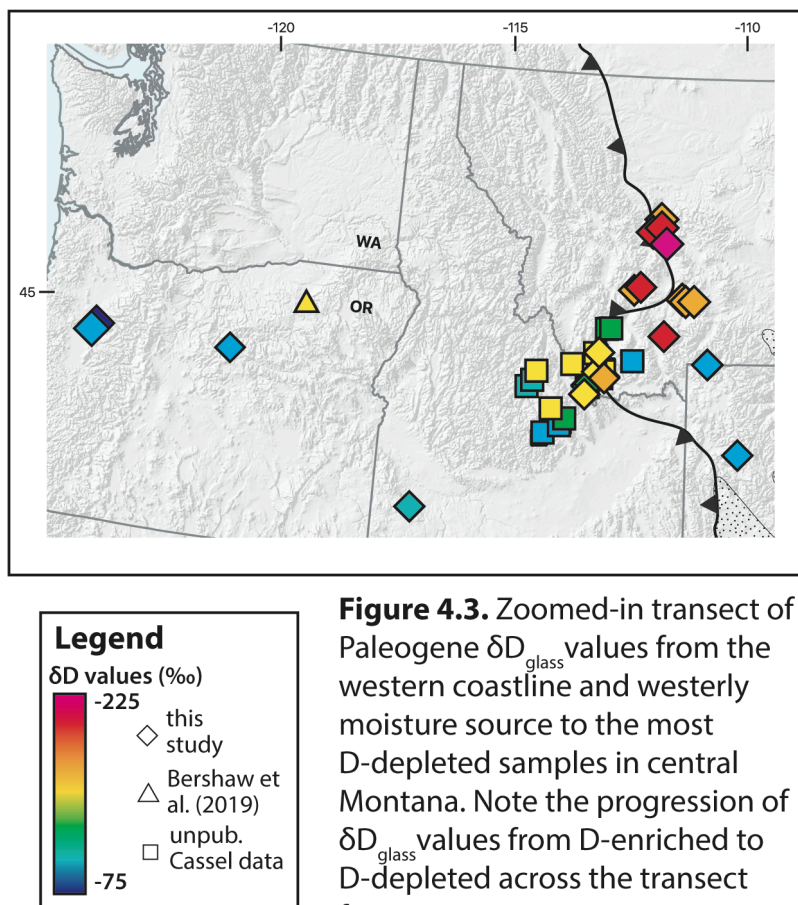
Figure 4.3. Zoomed-in transect of Paleogene δD_{glass} values from the western coastline and westerly moisture source to the most D-depleted samples in central Montana. Note the progression of δD_{glass} values from D-enriched to D-depleted across the transect from west to east.

4.3.1. Group WY

Samples WY20_444WB-A, WY19_345CP-A, 18WY_123SLT-D, and WU14_052WR-B are all located in Wyoming and exhibit comparable TREE patterns. This

group is depleted in Th, Sm, Y and Yb trace elements and moderately depleted in Ce. Group WY also exhibits moderate enrichment in the LREE and depletion in HREE. Additionally, these are the only samples enriched in Eu. Samples WU14_SCM-1 and WY19_338AB-B could also be included in this group. WU14_052WR-B is dated at 51.74 ± 0.09 Ma using sanidine ^{40}Ar/^{39}Ar (Smith et al., 2008).

4.3.2. Group WB

Three samples from the Wagon Bed Formation (WY20_450-452WB-A), also from Wyoming, and one western Montana sample (MT15_016CC) form this group. These samples have the smallest LREE enrichment, moderate Eu depletion, and a consistent, pronounced Th and Ta enrichment (378.42 – 719.24 ppm and 159.69 – 324.42 ppm, respectively). TREE concentrations tend to cluster closely with little intra-grouping variability. These units have land mammal dates of Uintan age (VanHouten, 1964).

4.3.3. Group WMT

Samples 18MT_129CR, MT20_464MC-A, and MT20_465MC-A form another group in western/southwestern Montana, however North Dakota samples ND20_402SB-A and ND20_404SB-A and B may be considered part of this subset. This group is depleted in Y and Yb, has a very small Eu depletion, and is moderately depleted in HREE, although less pronounced than Group WY. Samples WU14_SCM-1 and WY19_338AB-B could also be grouped with these samples. 18MT_129CR is dated as 53.1 Ma (K/Ar); MC samples are likely middle Eocene (Janecke et al., 1999); North Dakota samples are suspected to be late Paleocene in age (Table 1). WY19_338AB-B and WU14_SCM-1 are middle Eocene (48.89 ± 0.02 Ma – U/Pb and 47.45 ± 0.08 Ma – sanidine ^{40}Ar/^{39}Ar, respectively (Smith et al., 2008; Tsukui, 2016).

4.3.4. Group CMT

Six central Montana samples, 18MT_108LIVALN, 18MT_112VC-B, 18MT_114SC-B, MT20_424CF-B, and MT20_426CF-A,B, form a cluster that is enriched in Ba, Th, Zr, and Hf compared to other groupings. Samples have moderate Eu depletions and only slight LREE enrichment. Elemental concentrations display little variability within the group, but
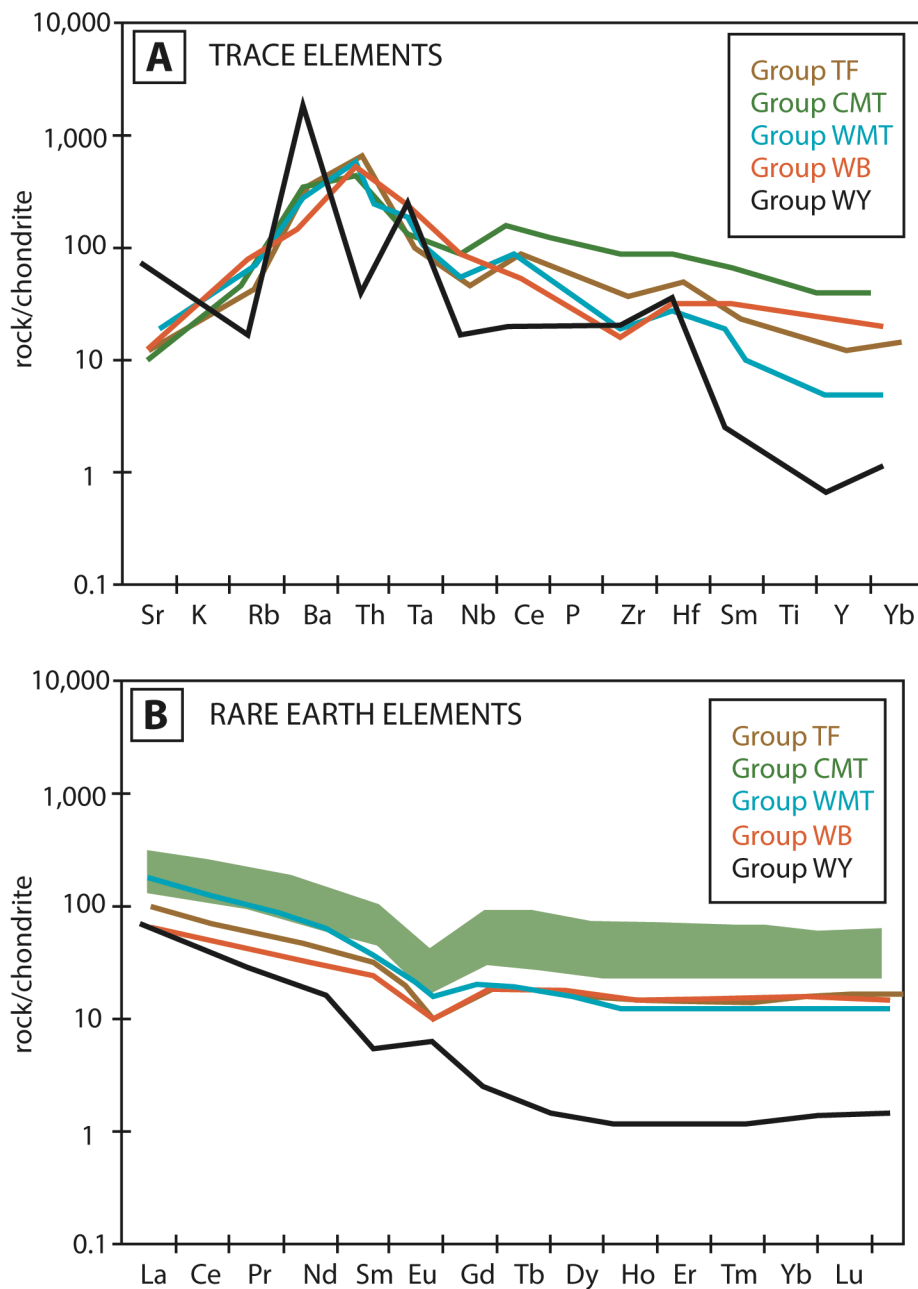
Figure 4.4. Spider diagram plots of A) trace element and B) rare earth element concentrations, normalized to chondrite values of McDonough and Sun (1995). No K or P results were returned. Samples are grouped by TREE pattern similarities (see Table 4.2).
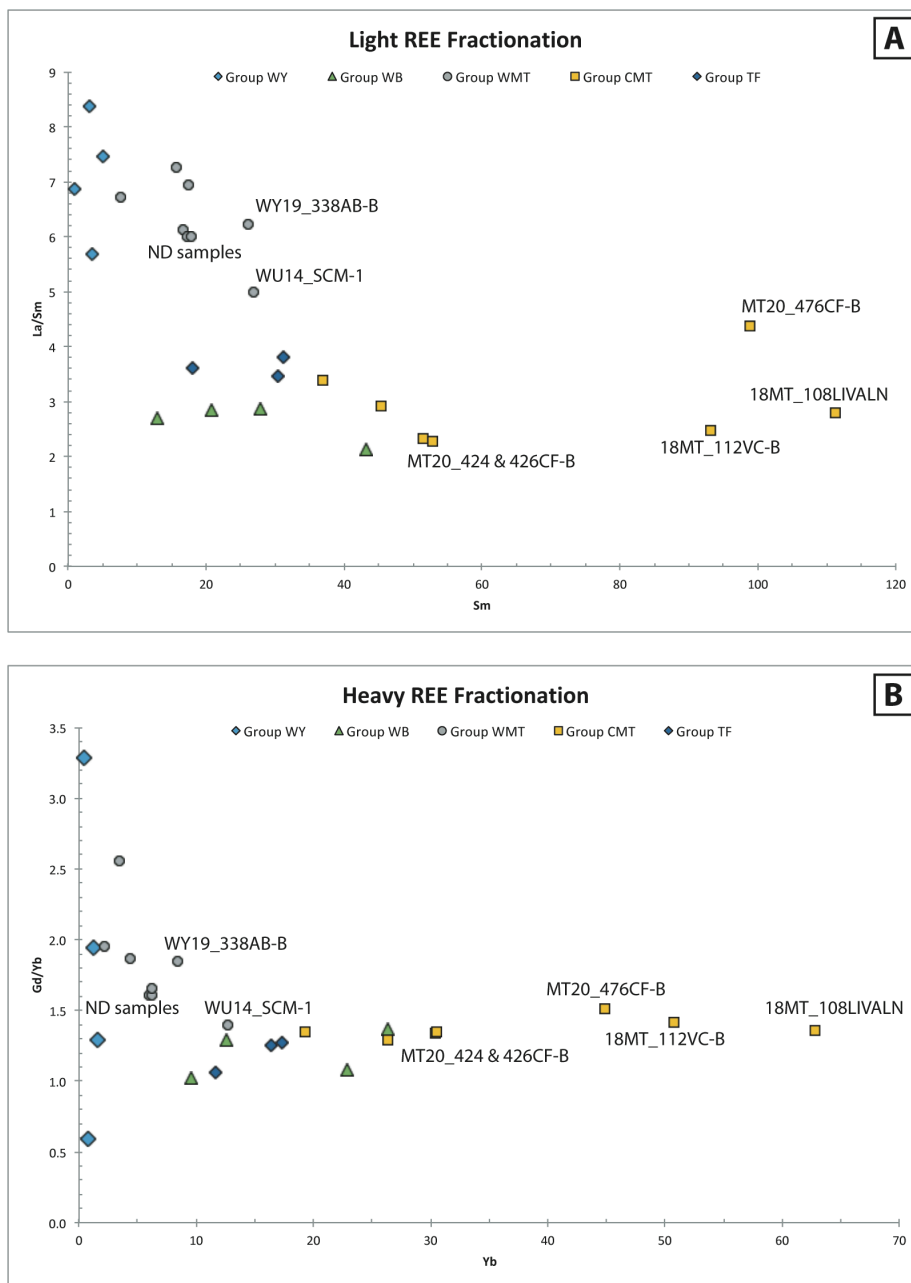
Figure 4.5. Rare earth element fractionation diagrams for A) light rare earth element fractionation, B) heavy rare earth element fractionation, and C) the Europium anomaly. Samples are divided based on spider diagram trend and TREE concentration similarities (see Table X). Note: samples WU14_SCM-1 and 19MT_338AB-B could fit into multiple groups, including groups WY, WMT, and CMT, but the closest fit is group WMT.
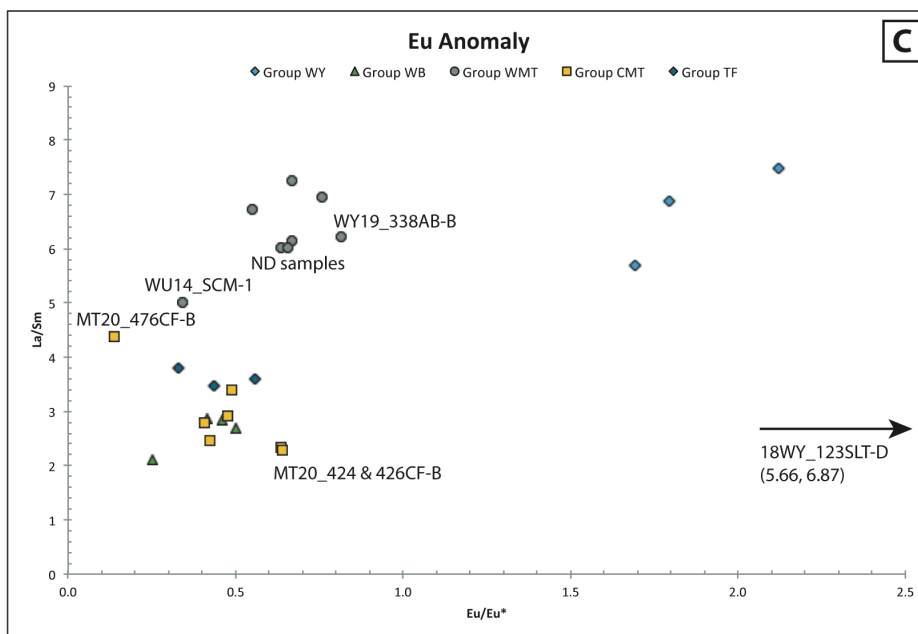
Figure 4.5, cont'd.

two sample pairs stand out as being highly similar with considerable overlap: 18MT_108LIVALN and 18MT_112VC-B; MT20_424CF-B and MT20_426CF-B. These four samples all have slightly less LREE enrichment, but still display a noteworthy similarity to the other two samples in the group. MT20_424CF-B and MT20_426CF-B TREE concentrations are within error of each other (Table A1). MT20_476CF-B may fit in this group, but has a very large Eu depletion that makes it stand out from the other samples from this area (Fig. 4.5). WU14_SCM-1 exhibits a similar (but slightly larger) LREE enrichment and moderate Eu depletion, making it a candidate for inclusion in this group. 18MT_108LIVALN, 18MT_112VC-B, and 18MT_114SC-B are dated at 53.1 Ma, 49.3 Ma, and 45.54 Ma respectively (Table 3.1). Canyon Ferry samples are Oligocene in age based on map correlations (Freeman, 1958; Vuke, 2011; McDonald et al., 2020).

4.3.5. Group TF

Three Jefferson-Three Forks Basin samples, MT19_344TF-A, MT20_JEFF[0], and MT20_JEFF[9], are Th-enriched with slight-to-moderate LREE enrichment and moderate Eu depletion. All three samples are latest Eocene – early Oligocene in age, based on Chadronian mammal ages of Tabrum et al. (2001) and correlation by Vuke (2003).

Table 4.2. Groupings of samples based on TREE similarities with inferred sources and distinguishing characteristics highlighted.

Grouping	Samples Included	LREE	HREE	Eu/Eu*	Other Notable Trends	Age Range (Ma)	Probable Source
Group WY	WY20_444WB-A WY19_345CP-B 18WY_123SLT-D WU14_052WR-B (WY19_338AB-B) (WU14_SCM-1)	moderately enriched	depleted	positive (other than AB and SCM samples)	depleted in Th, Sm, Y, Yb, Ce	52 - 45	intermediate: Absaroka and/or Challis
Group WB	WY20_450-452WB-A MT15_016CC	smallest enrichment of all groups	smallest depletion of all groups	moderately depleted	enriched in Th, Ta	43-47	Silicic Challis, 48-45 Ma
Group WMT	18MT_129CR MT20_464-465MC-A (ND20_402SB-A) (ND20_404SB-A,B) (WY19_338AB-B) (WU14_SCM-1)	moderately enriched	moderately depleted, but less so than Group WY	very small depletion	depleted in Y, Yb	~58 (ND) 53 - 43	intermediate: Challis, Lowland Creek (129CR)
Group CMT	18MT_108LIVALN 18MT_112VC-B 18MT_114SC-B MT20_424CF-B MT20_426CF-A,B (MT20_476CF-A)	slightly enriched	slightly to moderately enriched	moderately depleted (476CF-A highly depleted)	enriched in Ba, Th, Zr, Hf	53 - 45 35 - 21	Early-mid Eocene: lower Dillon, Lowland Creek, Challis Oligocene: middle Dillon Miocene: upper Dillon?
Group TF	MT19_344TF-A MT20_JEFF[0,9]	slightly to moderately enriched	slightly to moderately depleted	moderately depleted	enriched in Th	37 - 33	Felsic: middle Dillon

5. DISCUSSION
5.1. Modern δD_{water} Trends

δD_{water} values, when plotted versus longitude, show a distinctive saddle-shaped pattern (Fig. 5.1). Water samples are most D-depleted in the high topography of the modern Rocky Mountains and most D-enriched along the Pacific coast and in the Great Plains. δD_{water} values progressively decrease from the Pacific coast to the approximate modern crest of the Rockies in western Montana and western Wyoming. On the windward side of the Cascade Range and, to a lesser extent, between the Cascades and the Sevier fold-thrust front, is a clear inverse relationship between longitude and δD_{water} value, which also corresponds with a west-to-east increase in elevation (Figs. 3.2; 5.1). The observations in the modern Cascades provide a close fit to the modern global meteoric water line, which has a slope of 8 and an intercept of 10 (Fig. 5.2). The modern Cascades LMWL for all modern data is:

$$y = 7.7742x + 8.1288$$
$$R^2 = 0.967$$

Following the dominant airmass trajectory from west to east, δD_{water} values increase from the Rocky Mountain front to the Midwest. The most pronounced δD_{water} value changes occur east of the modern crest (Montana) and east of the Laramide province (Wyoming). Here, water δD values increase by ~60‰ over a short distance (<1° longitude). This drastic change roughly follows the locations of high topography, including the Bighorn Mountains of northeastern Wyoming. This saddle-shaped pattern observed in the modern δD dataset is is typical of areas containing an airmass mixing zone (Rowley and Garzione, 2007; Vachon et al., 2010). Vachon et al. (2010) identifies a zone of airmass mixing in the northern Midwest and Great Plains regions where D-depleted Pacific moisture traveling east mixes with relatively D-enriched vapor sourced from the Gulf of Mexico. East of the Rocky Mountain front, δD_{water} values reflect vapor contributions from both Pacific and Gulf sources (Fig. 4.1).

31
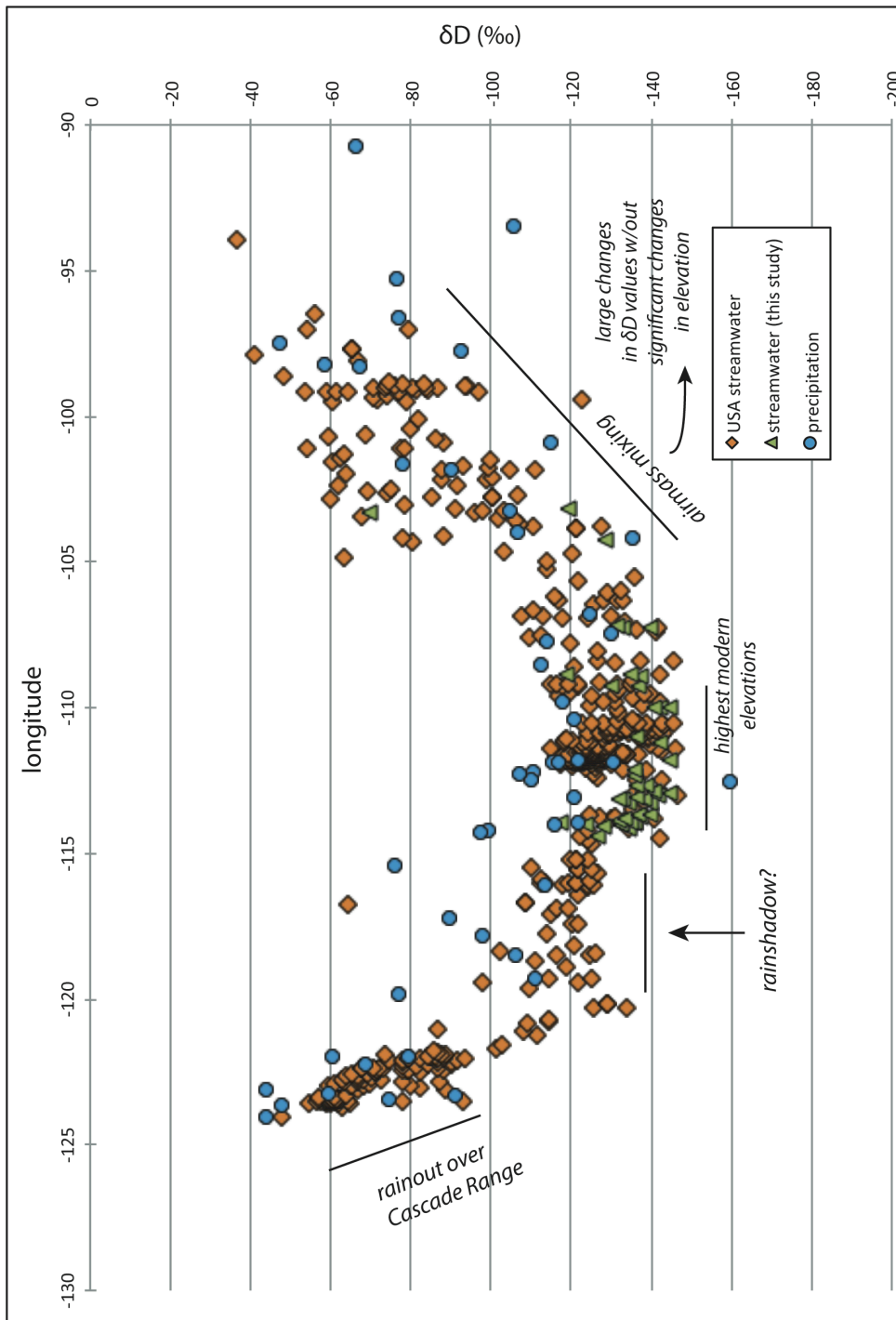
Figure 5.1. Plot of modern δD$_{water}$ against longitude between 40°N and 49°N. Symbology noted in legend. Modern δD values form a saddle shape typical of continents that experience airmass mixing to one side of high topography.
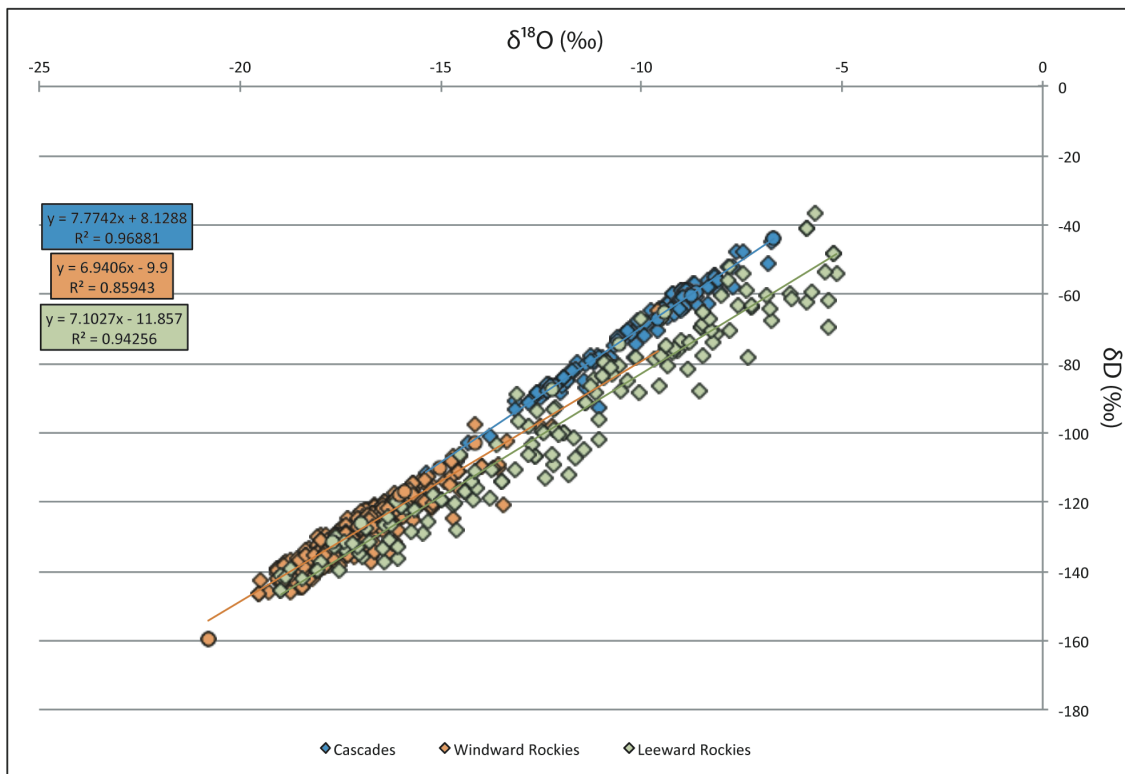
Figure 5.2. Plot of $\delta^{18}O$ vs. δD of modern stream (diamonds) and precipitation (circles) waters at ~45°N latitude. Stream waters analyzed for this study are denoted by triangles. Trendlines reflect local meteoric water lines for the Cascade Range, windward side of the Rocky Mountains, and leeward side of the Rocky Mountains are calculated. Data from this study, Waterisotopes Database (2020), and IAEA/WMO (2021). USNIP samples were only analyzed for δ18O values, so they were left out of LMWL calculations.

Airmass mixing is evident in scenarios where changing δD and $\delta^{18}O$ values cannot be attributed to other factors like adiabatic cooling, climate change, or progressive rainout over a landmass.

Differences in d-excess values can indicate different moisture sources and/or highly evaporative environments (Kendall and Coplen, 2001; Sharp, 2017). The most negative d-excess values across the study area are observed in the Great Plains (Fig. 4.1), and the most pronounced change in d-excess values (~5‰ to -10‰ from west to east) occurs in the same area as the sharp increase in δD_{water} values from west to east. Highly negative d-excess values are attributed to evaporative enrichment of deuterium during or after precipitation events, which is possible given the aridity of the western United States, but they may also indicate

atmospheric input from a separate moisture source, affecting the LMWL and revealing an airmass mixing signature (Zhu et al., 2018).

To assess the contributions of airmass mixing versus evaporation in the low d-excess values and relatively high δD_{water} values, I evaluated LMWLs for the Cascade Range and windward and leeward regions within the study area (Fig. 5.2). The LMWL slope on the windward side of the Rocky Mountains has the lowest slope of 6.94 with an intercept of -11.9, data points in the windward longitude range (109°W to 121°W) are represented by the equation:

$$y = 6.9406x - 9.9$$
$$R^2 = 0.859$$

The leeward side of the Rockies (90°W to 109°W) has a LMWL slope of 7.1 with an intercept of -9.9 – comparable to the windward side, following the equation:

$$y = 7.1027x - 11.857$$
$$R^2 = 0.943$$

The low slope and negative intercepts of the two LMWLs on either side of the mountain range suggest that the study region east of the Cascade Range is a moderately evaporative, consistent with the observations of other workers (Kendall and Coplen, 2001; Vachon et al., 2010; Sharp, 2017). However, even though the LMWLs indicate similar evaporative influences on δD_{water} values, the d-excess values are, on average, 7‰ less than they are west of the Sevier thrust front. The boundary between the two d-excess value regions is quite sharp, which could mean that A) sudden input of an additional moisture source is affecting δD_{water} and d-excess values or that B) spatially abrupt changes in amount of evaporation, typical of rainshadows and other areas whose climates are controlled by local high topography, are two possible processes affecting d-excess values (Fig. 4.1). Because drastic changes in leeward δD_{water} values occur over slight elevation changes, it is unlikely that sudden changes in evaporative potential are the culprit for the sharp boundary between D-depleted and D-enriched water values. The distance from the Gulf of Mexico to the edge

of the Wyoming Laramide province is ~1500 km (Rowley and Garzione, 2007), so the continentality effect (-24‰/1000 km on the δD scale) cannot produce the most enriched South Dakota δD_{water} value of -69.6‰ (Table 4.1). Instead, this zone is likely subjected to airmass mixing of westerly, highly D-depleted Pacific moisture that has passed over high topography with relatively D-enriched Gulf of Mexico moisture.

5.2. Modeled Paleoelevations

Samples from west-central and southwest Montana at the toe of the Sevier fold-thrust belt consistently have the lowest δD_{glass} values across the study area and all time slices, suggesting high topography here was sustained for at least 25 to 30 Ma (Fig. 5.3). These results indicate the general location of the Paleogene crest of the northern U.S. Cordillera, as the lowest δD values would either lie at the area of the highest elevations because all values further to the east and west reflect less D-depletion (Fig. 5.3). Based on the modeled paleoelevations, the progressive decrease in δD_{glass} values from Oregon to southwest and west-central Montana likely required rainout over elevations of at least 4.2 km in the early Eocene and 2.9 km by the middle Eocene to Oligocene. This differs from the conclusions of recent provenance studies that hypothesize central Idaho was a regional topographic high, due to the presence of Challis material in Wyoming basins among other large basins to the west (e.g., Tyee Basin, California Great Valley) that indicate extra-regional transport (Chetel et al., 2011; Dumitru et al., 2012). However, model results show that the highest elevations were in western Montana, not central Idaho, necessitating re-evaluation of drainage and regional transportation pathways (Figs. 5.3; 5.4). Model paleoelevation estimates for this study are given in Table 5.1.

5.2.1. The Late Paleocene and Early Eocene (58-50 Ma)

In the early Eocene, ca. 53 Ma, the most D-depleted samples from west-central and southwest Montana are the highest modeled paleoelevations in the study area at 4,640 $^{+720}/_{-440}$ m (Table 5.1; Fig. 5.4). To the south, a sample of the Halfway Draw Tuff (Wind River
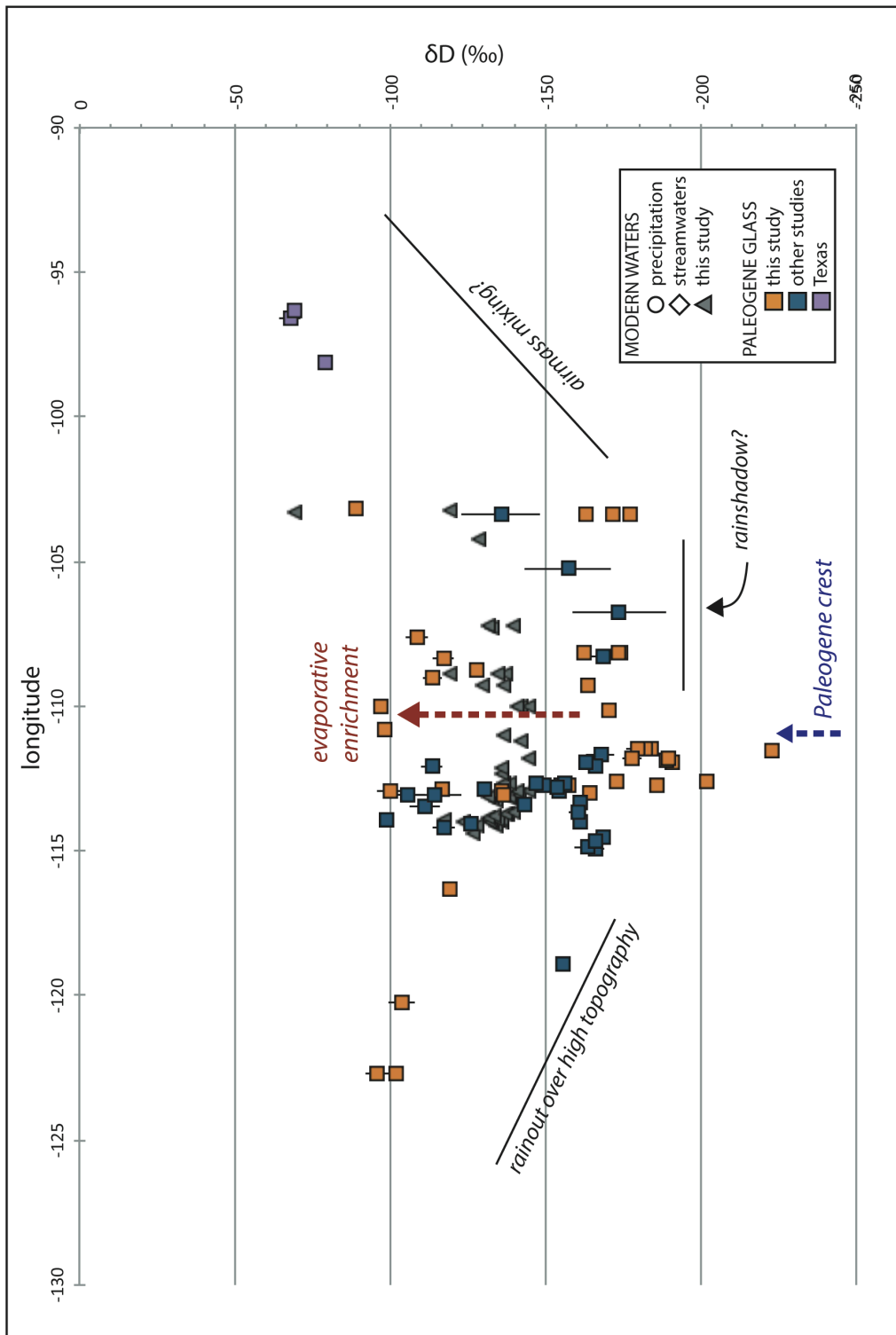
Figure 5.3. Plot of modern δD$_{water}$ and Paleogene δD$_{glass}$ against longitude. Symbology noted in legend. Modern δD values form a saddle shape typical of continents that experience airmass mixing to either side of high topography. Paleogene glass δD values have a slight saddle shape with longitude, but the effect is not as visible due to likely evaporative trends between -115° and -107° longitude. Texas samples from Cassel et al., 2009.

Table 5.1. Rainout model results.

Sample No.	Distance From Modern Shoreline (km)	Modeled Elevation (m)	Lower Error (m)	Upper Error (m)
OR21_505WV*	115.7	410	-45	46
OR21_506WV*	115.7	196	-28	11
16OR_003JD	304.6	710	-81	90
18ID_104PC	662.5	1561	-168	187
18MT_129CR	865	4615	-379	632
MT20_464MC-A	870.35	2301	-229	264
MT15_016CC	870.42	3345	-296	332
MT20_465MC-A	875.47	1430	-160	178
18MT_108 Liva Ln-A	875.5	4584	-380	632
WU14-048MC-A*	876.9	534	-64	73
18MT_113GLEN-B	879.3	3109	-280	315
MT15-008SC	883.4	3101	-272	315
18MT_114SC-B	897.8	3612.5	-313	348
WU14_012ML	919.3	2088	-194	149
MT20_424CF-B	928.5	3145	-250	276
MT20_426CF-A	938	3153	-250	276
MT20_426CF-B	938	2907	-233	260
18MT_112VC-B	938.9	4722	-380	640
MT20_476CF-B	957.9	3826	-290	309
MT20_JEFFSEC[0]	966.1	3594	-294	329
MT19_344TF-A	966.1	3563	-302	329
MT20_JEFFSEC[9]	966.1	3516	-294	329
18MT_117GR-A*	1033.6	1436	-160	278
18WY_123SLT-D*	1096.3	1290	-142	161
WY19_338AB-B	1129.5	257	-37	38
WU14_SCM-1	1166.4	3534	-313	340
UT15_033DP	1238.8	2528	-209	235
WY19_345CP-B	1278.4	1945	-203	230
WU14-052WR-B	1280.2	1593	-178	304
WY20_452WB-A	1295.2	3628	-313	356
WY20_451WB-A	1295.4	3659	-313	348
WY20_450WB-A	1295.5	3290	-296	324
WY20_444WB-A*	1316	1050	-125	135
ND20_404SB-A	1567.6	3911	-339	575
ND20_404SB-B	1567.6	3447	-330	559
ND20_402SB-A	1570.1	3456	-306	534
SD20_406BL*	1615.8	7	-	-

* high water content

Formation), WU14_052WR-B (51.74 Ma; Smith et al., 2008), in the Wind River Basin has a modeled paleoelevation of 1600^{+304}_{-180} m but also has a high-water content of 9.93 wt. % (Table 3.1). While this could indicate a potentially evaporative lacustrine source likely to enrich hydration waters in deuterium (Cassel and Breecker, 2017), the Wind River Formation depositional environment was alluvial, requiring an alternative chemical or environmental explanation (Smith et al., 2008).

To the east, in the late Paleocene (ca. 58 Ma) plains of North Dakota, average paleoelevation estimates are 3400 $^{+555}/_{-320}$ m, modeled using initial temperatures roughly equivalent to those of the late Eocene (Zachos et al., 1994). These samples are approximately 5 Ma older than the other early Eocene samples in the study (Table 3.1). Here, δD_{glass} values range from -163‰ ± 0.9‰ to -177‰ ± 0.2‰, which is 10-22‰ greater than those found in west-central and southwest Montana. Three scenarios, or combinations thereof, could explain the difference in δD_{glass} values between the fold-thrust belt and the foreland in the early Eocene: evaporative enrichment, airmass mixing, or climate change. The Great Plains most likely occupied low elevations at the time, as the region was blanketed by a transitional to swampy terrestrial environment, indicated by Fort Union Group strata, interpreted as a low-elevation deltaic plain of the Cannonball Sea, which is supported by field observations of very fine sand and silt layers with some organic material (Clayton et al., 1980; Lisenbee, 1988; Fahrenback and Sawyer, 2011). Instead of changes in elevation, these δD_{glass} values may reflect mixing of D-depleted moisture originally sourced from the Pacific with moisture sourced from the Gulf of Mexico. Moisture sourced from the Gulf has higher initial δD values due to decreased fractionation in warmer climates. Ice-free ocean temperatures increased by ~5°C from 58 to 53 Ma, which would have decreased the early Eocene liquid-vapor fractionation factor relative to the late Paleocene (Zachos et al., 1994; 2008).

5.2.2. The Middle Eocene (49-43 Ma)

Middle Eocene (49-43 Ma) paleoelevation estimates are highest in southwest Montana, particularly in the Sage Creek Basin (Fig. 5.4), where estimates average 3450 $^{+320}/_{-300}$ m. In the nearby Muddy Creek basin, there is more variability in δD_{glass} values and paleoelevation estimates between different stratigraphic levels in the basin. Samples yield paleoelevations between 3350 $^{+330}/_{-300}$ and 540 $^{+70}/_{-60}$ m. Because of the presence of much lower δD_{glass} values in neighboring basins and within other stratigraphic levels within the Muddy Creek basin, it is unlikely that the D-enriched samples from Muddy Creek are reflective of paleoprecipitation and are instead indicative of evaporative intervals in an ancient lake (Smith et al., 2017). Schwartz et al. (2019) and Thoresen and Cassel (2020) document lacustrine organic mudstones and lignites interbedded with coarser fluvial sediments. Fossiliferous carbonate beds, carbonaceous shales, and lacustrine gastropod

coquinas all support the interpretation that a stratified lake occupied the basin at times (Janecke et al., 1999; Thoresen and Cassel, 2020), providing an environment for evaporative enrichment of surface waters. The high water contents (>9 wt. %) of WU14_048MC-A and MT20_465MC-A lend support to this hypothesis, as lake-hydrated glasses typically have higher water contents (Cassel and Breecker, 2017). Central Idaho δD_{glass} values (-152 ± 8‰) yield modeled elevations of 3 − 3.5 km (Fig. 5.4). These elevations are in agreement with previous paleobotany studies that estimated hinterland elevations of 3 − 4 km (Axelrod, 1965; Wolfe, 1994). In the Wind River basin, Wagon Bed formation samples, ca. 46 Ma, yield modeled paleoelevations of 3420 $^{+540}/_{-520}$ m. D-enriched samples elsewhere in the Wind River, Bighorn, and Green River Basins yield lower paleoelevations (<2000 m).

5.2.3. The Late Eocene and Oligocene (42-25 Ma)

A late Eocene sample from the John Day Formation (39.1 Ma) in Oregon has a δD_{glass} value of -104‰ and yields a best estimate paleoelevation close to modern elevations (710 $^{+90}/_{-80}$ m). Montana's Jefferson-Three Forks Basin samples of late Eocene age (37-33 Ma) have an average modeled paleoelevation estimate of 3560 $^{+330}/_{-300}$ m.

Oligocene samples are most D-depleted in central Montana in the Canyon Ferry area. Best estimate paleoelevations from MT20_424CF-B and MT20_426CF-A,B in this area are 3070 $^{+270}/_{-245}$ m. Low-elevation samples OR21_505-506WV in western Oregon are relatively D-enriched compared with most other samples. Both elevation estimates are <500 m, and the 506WV sample is used as the low-elevation datum. One Oligocene Bishop Conglomerate sample in Vernal, UT records a modeled paleoelevation 2530 $^{+235}/_{-210}$ m. Similarly, sample SD20_406BL from northwestern South Dakota, collected from the White River Group (latest Eocene to Oligocene), has a δD_{glass} value of -88.9 ± 2.2‰ with a paleoelevation estimate of 7 m, far below the modern average elevation of the area of 930 m. This sample was collected in a tuffaceous siltstone, lightly reworked into laminations with flat bedding. Combined with a high water content of 10.37 wt %, this sample is likely to have been deposited in or near an evaporative lacustrine setting (Cassel and Breecker, 2017). If this is not the case, the high δD_{glass} value provides a strong indication of input by an additional moisture source.
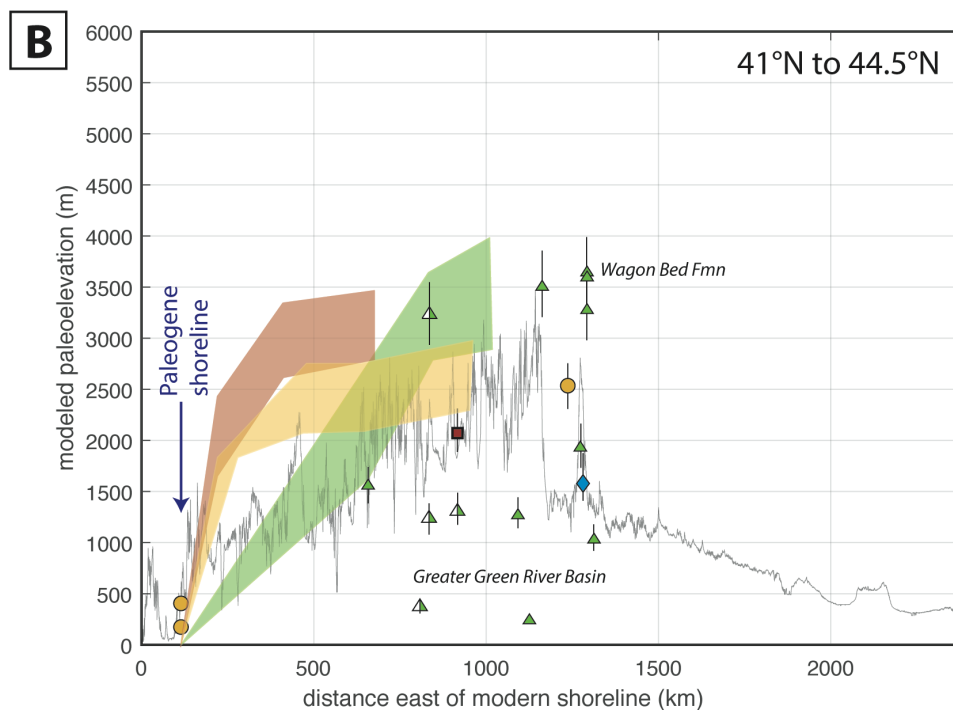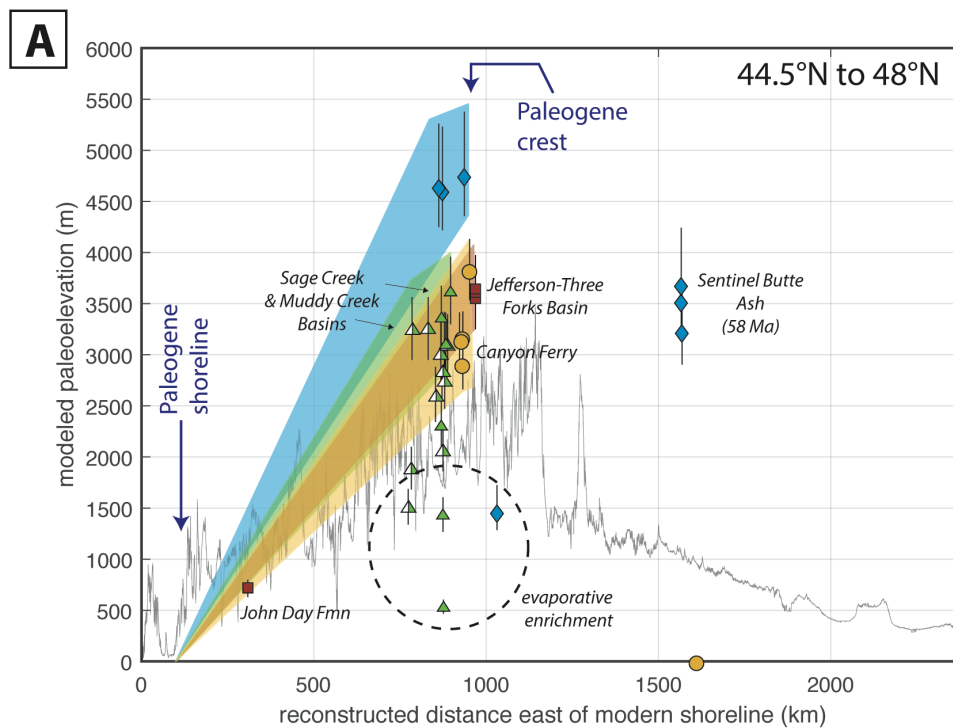
Figure 5.4. Plot of modeled paleoelevations against modern elevation profile at A) 44.5°N to 48°N and B) 41°N to 44.5°N. Error bars incorporate 2σ error from glass δD measurements. Shaded areas are interpreted topographic profiles (within 2σ). Half-shaded points from Cassel, unpub. Late Eocene and early Oligocene profiles in (B) from Cassel et al., 2018.
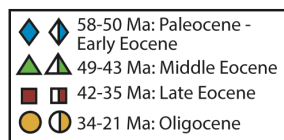
5.2.4. Paleoclimate Implications

Pacific-sourced moisture likely composed the dominant airmass trajectory across the orogenic belt in the Eocene, as it does in the modern wet season (Vachon et al., 2010). This is seen in the clear decrease in modern and paleo δD values between the western shoreline and the Cordilleran crest (Fig. 5.3). The low δD$_{glass}$ values at the toe of the Sevier fold-thrust belt cannot be attributed solely to latitude, temperature, or continentality effects. The continentality effect could account for ~20‰ over the reconstructed 750 km distance (δD scale), using approximated extension of 30% in the Rocky Mountain Basin and Range since the Oligocene (Coney and Harms, 1984; Gilbert, 2012). To hypothetically achieve such low ΔδD values via climate change and/or continentality, a 19°C decrease from the initial Eocene MAT of 20-25°C would be required. This is unreasonable given scientific agreement establishing the early Eocene hothouse climate (Zachos et al., 2008; Poulsen and Jeffery, 2011; Huber and Caballero, 2011. Therefore, the progressive D-depletion seen in this dataset from west to east can only be explained by airmass rainout from the paleo-Pacific shoreline over the western flank of the Eocene Rockies.

Windward and leeward δD$_{glass}$ value comparisons for a given time slice highlight the Eocene rainshadow. If there is moisture recycling and no airmass mixing on the leeward side of a mountain range, δD$_{glass}$ values should show minimal change with distance east of the lowest values, as is the case in the modern Basin and Range province of Nevada (e.g., Mulch, 2016; Cassel et al., 2018). δD$_{glass}$ values may show a subtle decrease due to the continentality effect, although this would only account for a change of only -2.4‰ over 100 km of distance (δD scale) (Ent et al., 2014; Sharp, 2017). Though modern δD$_{water}$ values experience a change of -8‰ per degree of latitude gained due to temperature decreases, it was likely only negligible changes in temperature existed across the mid-latitudes during the Eocene due to high pCO$_2$ (Poulsen and Jeffrey, 2011; Sharp, 2017). Modern δD values reflect an increase in δD value with increasing distance east of the Sevier thrust front (Fig. 5.1), typical of airmass mixing (Vachon et al., 2010).

From the Eocene to the Oligocene, there is an increase in the windward lapse rate from -20‰/km of elevation gain (central Oregon to west-central Montana) to -31‰/km of elevation gain (western Oregon to Canyon Ferry, Montana). This is likely the result of the

well-documented global cooling across the Eocene-Oligocene Transition. The smaller, opposite effect of lapse rate moderation due to a climate drying-related decrease in RH is negligible based on model sensitivity to the RH parameter (Fig. 3.4; Rowley, 2001; Kent-Corson et al., 2006; Anagnostou et al., 2016). In warmer time periods, like the Eocene, lapse rates are shallower due to the inverse relationship between initial temperature and fractionation because cooler temperatures drive more rainout (Dansgaard, 1964; Rowley, 2001). High pCO2 also dampens lapse rates due to increased initial surface and atmospheric temperatures (Poulsen and Jeffery, 2011). On the leeward side of the mountains, the Eocene δD lapse rate is -8.5‰/km of elevation gain from east (North Dakota) to west (west-central Montana). Similarly, the Oligocene lapse rate, using an eastern point in Nebraska from Fan et al. (2014), is -21‰/km of elevation gain.

5.3. Composition and Correlation of Tuffs

Due to the abundance of Eocene and Oligocene volcanic centers in the western U.S., tephrochronology is useful in the correlation of glass-bearing volcanic and volcaniclastic rocks with identified volcanic centers. Identification of source regions makes reconstruction of distribution patterns, both ground and atmospheric, possible. TREE concentration patterns are summarized in Table 4.2. Drainage and air travel trajectories are interpreted in Figure 5.5.

5.3.1. Identification of Likely Volcanic Sources

Group WY, containing samples from Eocene central Wyoming, displays compositions typical of an intermediate magma source. These samples are enriched in Eu, indicating that plagioclase had not yet crystallized, so the samples were derived from less-evolved magma than those in other groupings (Rollinson, 1995). A large HREE depletion also suggests an intermediate magma composition (Rollinson, 1995). Based on proximity and geographic position of sample localities to the Challis and Absaroka volcanic fields, sample composition, and early-middle Eocene sample ages, these large volcanic centers are both possible sources for this group. Even though volcanic centers within both volcanic provinces were erupting silicic and intermediate material during this time, closer proximity to the Absaroka volcanic field and dominance of intermediate compositions make them a likely

source, although Challis materials are often found in Greater Green River Basin strata (Chetel et al., 2011; Dumitru et al., 2012).

Group WB has a felsic geochemical signature based on samples' degrees of Eu depletion (Fig. 4.5; VanHouten, 1964). Though all samples in this group are Eu-depleted, the magnitude of this depletion varies due to magma evolution over time, with the largest Eu depletion found in WY20_452WB-A, the youngest sample taken based on stratigraphic superposition (Rollinson, 1995). This could indicate evolution of a primary volcanic center towards greater degree of crustal assimilation and more felsic eruptions over time. Silicic Challis volcanism at 48 – 45 Ma is a probable source based on these observations and the middle Eocene age of the samples (Janecke and Snee, 1993; Sanford, 2005).

Group WMT samples all have moderate HREE depletion and individual Y and Yb depletions, indicating they are derived from volcanic centers with intermediate magmatic compositions (Table 4). Janecke and Snee (1993) and M'Gonigle and Dalrymple (1996) interpret Muddy Creek volcaniclastics as Challis-sourced tuffs. Sample WY19_338AB-B is geochemically similar to the Muddy Creek samples MT20_464MC-A and 465MC-A and could reasonably have a Challis signature, too. This is consistent with previous workers' identification of Challis-age material in the Greater Green River Basin (Chetel et al., 2011). However, WMT samples ND20_402SB-A and 404SB-A,B and MT18_129CR predate Challis volcanism. MT18_129CR was likely sourced from the intermediate Lowland Creek volcanic group based on a ^{40}Ar/^{39}Ar age of 53.1 Ma (Dudas, 2010). The ~58 Ma samples from the North Dakota Sentinel Butte Member of the Fort Union Formation have an intermediate volcanic source, though no researchers have positively identified the volcanic source of the Sentinel Butte ash bed (Li and Fan, 2018).

Group CMT has a more evolved magmatic signature, likely derived from a felsic volcanic source. However, the variety of sample ages in this group (53-25 Ma) suggest input from Lowland Creek and Dillon volcanic centers and/or later Challis activity. Of these six samples, MT20_424CF-B and MT20_426CF-B closely overlap, indicating a similar eruption age (Oligocene) and source. CMT Oligocene samples are too young to be derived from the Lowland Creek volcanics, leaving a northeasterly distribution of middle Dillon material (34-27 Ma) as the remaining possibility for a shared volcanic center source (Fritz et al., 2007). 18MT_108LIVALN and 18MT_112VC-B display similar TREE spider diagram patterns, but

with greater Eu depletion. These similarities suggest that these samples may also be sourced from the lower Dillon or Lowland Creek volcanic fields.

Group TF samples were taken at the same location in the Jefferson-Three Forks Basin at different stratigraphic levels. The similarities in elemental concentrations and spider diagram patterns suggest a common volcanic source, especially in JEFF[0] and JEFF[9]. Chadronian mammal ages show these reworked tuffaceous sandstones are latest Eocene to early Oligocene in age (Tabrum et al., 2001). The only active volcanic centers active at this time were the middle Dillon volcanic field to the west or the far-afield late Eocene – Oligocene Nevada ignimbrite flare-up to the southwest. Despite being hundreds of kilometers away, the large size and output of the Nevada volcanics makes it a potential contributor of air-fall material to these samples despite The presence of a thick (10 cm) airfall bed, in contrast to the tuffaceous sandstone facies elsewhere at the outcrop, is potentially the result of a nearby middle Dillon eruption.

5.3.2. Interpretation of Tuff Transport Patterns

Through ignimbrite and air-fall tuff correlation to regional volcanic centers and field identification of samples, I interpret patterns of extra-regional transport of volcanic debris via airmass trajectories and ground travel. Ash-fall tuffs, transported aerially by atmospheric rivers, help identify dominant atmospheric circulation patterns around and over high topography. Ignimbrites and welded tuffs are deposited by ground-traveling pyroclastic flows capable of traveling hundreds of kilometers (Hildreth and Mahood, 1985).

Analyzed samples from this study in both Montana and Wyoming are a mix of ignimbrites and ash-fall tuffs, and ground and air transport follow similar paths. Eocene samples from southwest Montana are found close to Eocene volcanic centers and are likely to be sourced from those same centers, while many samples in Wyoming and west-central Montana are sourced farther afield. Ash-fall tuffs and ignimbrites in the Wind River and Green River basins in central and southwest Wyoming (Groups WY, WMT, and WB) are interpreted as Challis and/or Absaroka in origin (Table 5.1). Ground transport from the Challis volcanics may have followed the Cretaceous drainage of the Harebell-Piñon megafan into the Wind River and Green River basins, consistent with the hypotheses of Janecke et al. (2000) and Carroll et al. (2010) (Fig. 5.5). This provides additional evidence that central
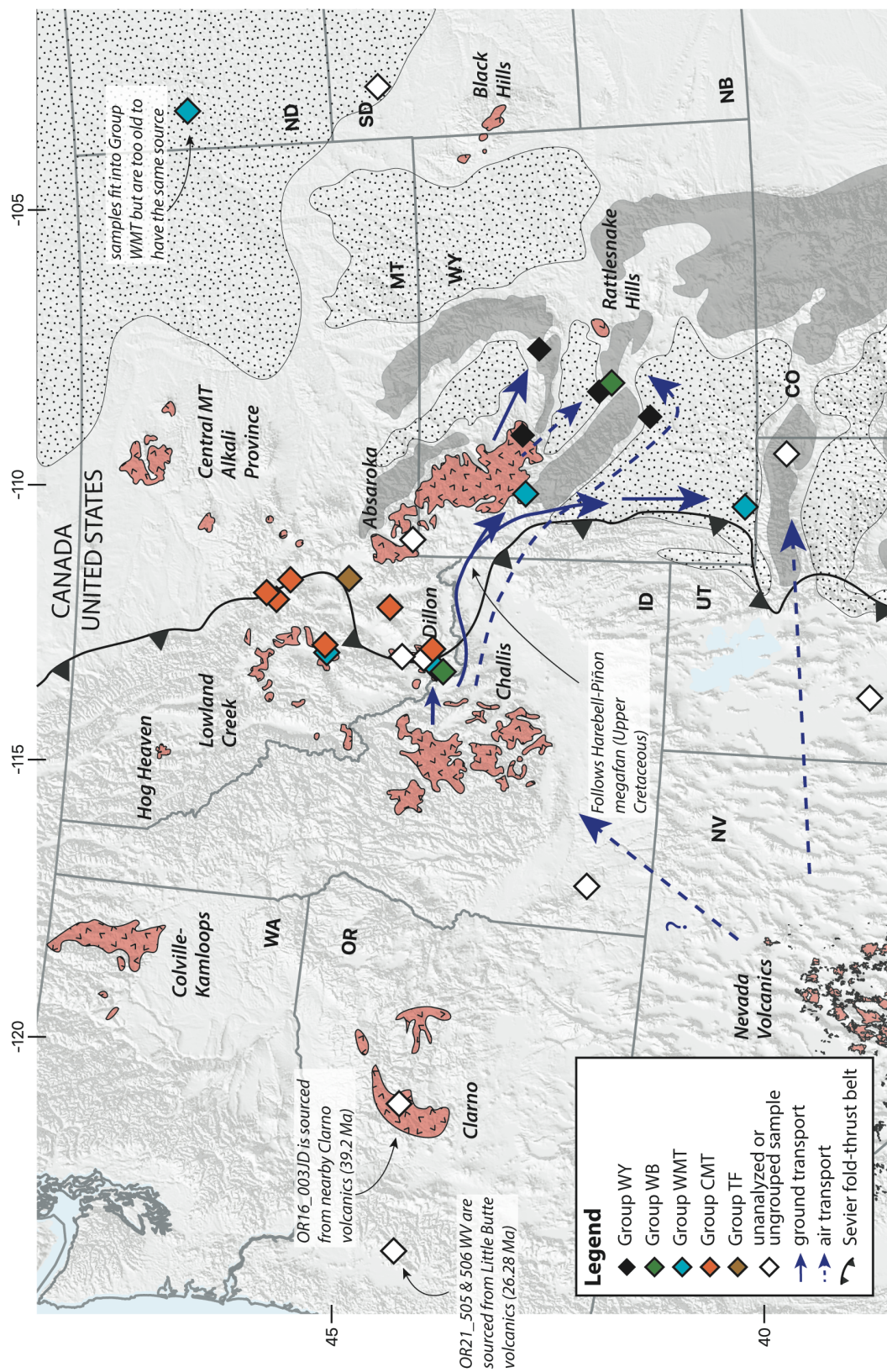
Figure 5.5. Map of proposed drainage and air circulation patterns based on TREE results.

Idaho was at a higher elevation than the foreland into the Eocene. Air transport likely followed a west-to-east trajectory to deposit volcanic debris, as has been found with global climate model simulations (Feng et al., 2013). Group WB, interpreted as Challis-sourced ash-fall with minor reworking, could have been deposited anywhere along the drainage system, potentially circumnavigating Laramide uplifts via air or fluvial transport (Fig. 5.5; 5.6).

5.4. Tectonic Implications of High Topography

5.4.1. Potential Mechanisms of Support for Paleogene High Elevations

Present crustal thicknesses in west-central/southwestern Montana are ~37 km (Gilbert, 2012). Extension throughout the Cenozoic resulted in crustal thinning of 15 – 50% in the western Montana and eastern Idaho in the early to middle Eocene and Neogene, seen in the formation of extensional basins and estimated from metamorphic core complex and Sevier fold-thrust belt reconstructions (Coney and Harms, 1984; Janecke, 1994; Foster et al., 2010). Basic Airy isostatic calculations using these new elevation estimates and approximate densities can be used to reconstruct crustal thicknesses to characterize the U.S. Cordilleran tectonic setting (Fig. 5.7) (Dickinson et al., 1988; Dickinson, 2004; Snell et al., 2014). These calculations are based on an end-member scenario that assumes surface uplift is attributed solely to the isostatic effects of thickened crust. This basic model is highly sensitive to changes in density, highlighting the importance of accurate estimates of lithospheric densities in tectonic interpretations.

The thickest crust is hypothesized to have occupied the area of the fold-thrust belt and hinterland where MCCs formed, so crustal thicknesses of 50-55 km are assumed in the locations of highest modeled paleoelevations to the east along the toe of the Sevier fold-thrust belt. Assuming a crustal density of 2.75 g/cm^3 and a mountain range height of 4.2 – 5.2 km in isostatic equilibrium with the western Great Plains, which has a current crustal thickness of 45 km at 2.85 g/cm^3 (Fig. 5.7) (DeCelles, 2004; Gilbert, 2012; Levandowski et al., 2018). Mantle asthenosphere density is estimated at 3.22 g/cm^3 (Levandowski et al., 2018). If crustal thickness was solely responsible for supporting high topography, the crust beneath the toe of the fold-thrust belt would be ~73 km thick. This is thicker than previous palinspastic reconstructions and other thickness estimates (e.g., Coney and Harms, 1984; DeCelles, 2004; Snell et al., 2014). Alternatively, to support 5 km elevations, crustal

densities would need to be 2.56 – 2.62 g/cm^3, which is lighter than cooled felsic igneous rocks or average crustal densities (Snell et al., 2014). Crustal thicknesses of 50-55 km would support 1.9 – 2.8 km of high topography, leaving 2.2 – 3.1 km of surface uplift to be achieved through other means.

Figure 5.6. Map series depicting interpreted locations of Paleogene high topography for each time slice. Estimates made based on model results, results from other studies, and known low elevation areas (e.g., Fort Union Formation).
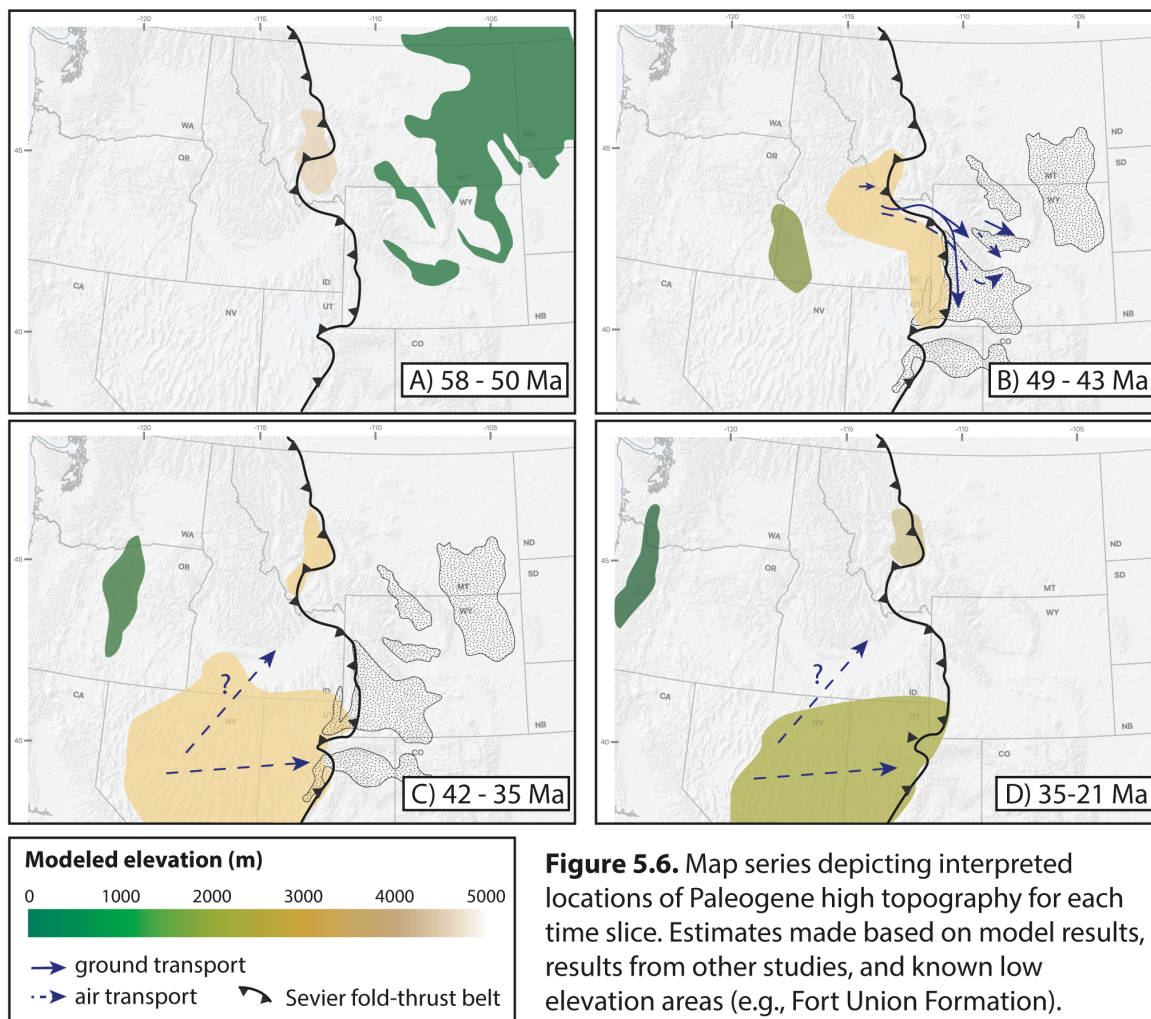
Other density-related factors that influence surface elevations are thermal uplift, mantle processes such as delamination and dynamic topography, and mineralogical changes such as crustal hydration (Canavan et al., 2014; Hyndman, 2015; Jones et al., 2015). An alternative end-member scenario of regional uplift is the creation of topography resulting entirely from thermal uplift. Possible mechanisms include heating of previously hydrated crust via 1) high heat flow driven by extension and decompression melting or 2) lithospheric delamination and thermal weakening (DeCelles, 2004; Humphreys, 2015; Jones et al., 2015;

Smith et al., 2017; Cassel et al., 2018). Hyndman (2015) cited the lack of modern crustal root in the southern Canadian Rocky Mountain highlands to suggest that crustal thickening is not the main driver of high topography in Cordilleran orogenesis. Hyndman instead proposed that thermal uplift, with a predicted heat flow of 55-65 mW/m^2, was the driving force behind modern Rocky Mountain elevations, accounting for maintenance of Canadian Cordilleran elevations of 1.6 km above those of the foreland basin. Porter (2016) used mid-crustal velocities to identify areas of high heat flow, potential lithospheric destabilization, and extension that would have resulted in thermally driven uplift. The amount of surface uplift possible due to thermal effects is debated, and hypotheses include: <1.0 km in the Oligocene in central-eastern Nevada during the ignimbrite flare-up (Cassel et al., 2014, 2018; Canada et al., 2019), ~1.0 km in middle Eocene northern Montana (Fan et al., 2021), 0.4 – 1.4 km in the western Great Plains since 125 Ma (Humphreys, 2015), 2.5 km in the early to middle Eocene Sevier hinterland of Idaho (Chamberlain et al., 2012), or between 0.2 and 0.6 km of uplift within 20 Ma of 20% lithospheric thinning (Levandowski et al., 2018).
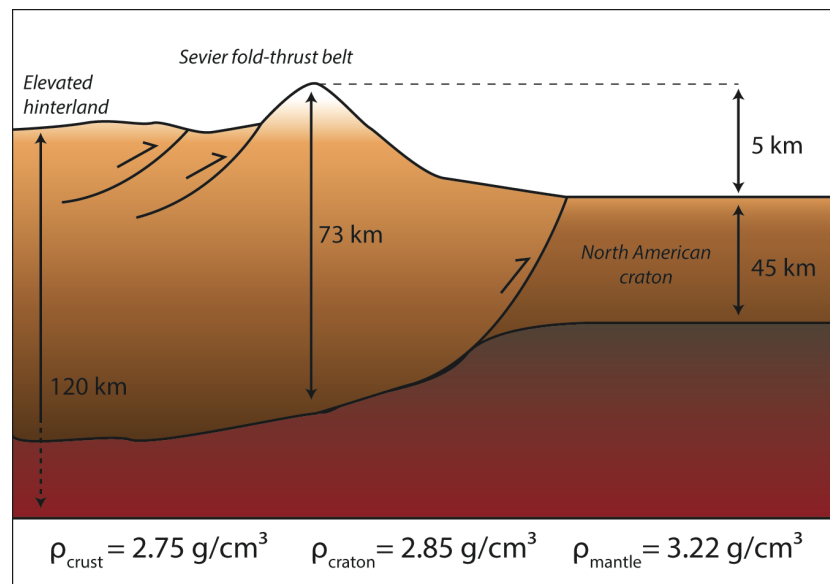
Figure 5.7. Schematic cross-section of the early Eocene Rocky Mountains with parameters used for simple isostatic calculations and end-member crustal thickness needed for 5 km of surface uplift. Not to scale.

5.4.2. Hypothesis for the Support and Creation of High Topography

The mechanisms of creation and support of northern U.S. Cordilleran high topography are most likely a combination of the thermal uplift and crustal thickening end members. Because at least moderately high topography (>2.8 km) persisted from the early Eocene into the Oligocene, mechanisms of support from high elevations must include one that is long-lived and independent of volcanic activity, which wanes in southwest Montana by the late Eocene. Reconstructed crustal thicknesses of 50-60 km along the Cordilleran fold-thrust are widely accepted and would have helped to support high topography (Coney and Harms, 1984; DeCelles, 2004; Cassel et al., 2014; Snell et al., 2014; Yonkee and Weil, 2015). Pre-extensional hinterland high elevations are generally thought to be 2-4 km (Axelrod, 1968; Wolfe et al., 2000; Snell et al., 2014).

However, the coincident occurrence of high heat flow due to intense volcanic activity with development of high topography, extension, and MCC exhumation should not be overlooked, making a thermal component to surface uplift likely. Magmatism in the western U.S. Cordillera was renewed with Lowland Creek volcanism ca. 53 Ma, contemporaneous with initiation of Anaconda MCC detachment and footwall exhumation (Fig. 2.1; Dudas, 2010; Foster et al., 2010). Similarly, Challis and lower Dillon volcanism coincide with extensional basin formation in southwest Montana (Lemhi Pass paleovalley, ca. 49 Ma) (Janecke and Snee, 1993; Janecke, 1994; M'Gonigle and Dalrymple, 1996; Janecke et al., 1999; Fritz et al., 2007). Concomitant extension and volcanism are capable of crustal thinning and decompression melting resulting in thermal uplift, but there is also strong evidence for the influence of north to south Farallon slab rollback. South-migrating topography, volcanism, and MCC exhumation consistent with the location of the slab hinge fits with progressive Farallon slab removal through the Cenozoic (Humphreys et al., 2003). Farallon slab de-watering during rollback hydrated the overlying crust, lowering the liquidus and initiating regional volcanism (Humphreys et al., 2003; Yonkee and Weil, 2015; Porter, 2016; Canada et al., 2019). Delamination of cold, dense mantle lithosphere and removal of high-grade metamorphic materials or mineral phases from fractional crystallization could also have triggered additional uplift (Jones et al., 2015; Porter et al., 2016; Smith et al., 2017).

Early Eocene (53-50 Ma)

A

Airmass trajectory

Sevier hinterland

Lowland Crk.

Challis

Absaroka

5 km

109°W
46°N

partitioning of foreland and initiation of basin ponding

44°N
118°W

localized shortening and/or extension

detachment faulting initiated

delamination and uplift?

uplift from thick crust and high heat flow?

Farallon slab

asthenospheric upwelling

Farallon slab rollback from N-S

Late Eocene to Oligocene (42-25 Ma)

B

3 km

109°W
46°N

Bitterroot & Anaconda MCCs

Dillon

hinterland extension

44°N
118°W

extensional basin formation and filling in SW Montana

uplift from possible delamination

lowering from crustal thinning and lower heat flow

Legend

basins

volcanic centers

metamorphic core complexes

Sevier fold-thrust belt

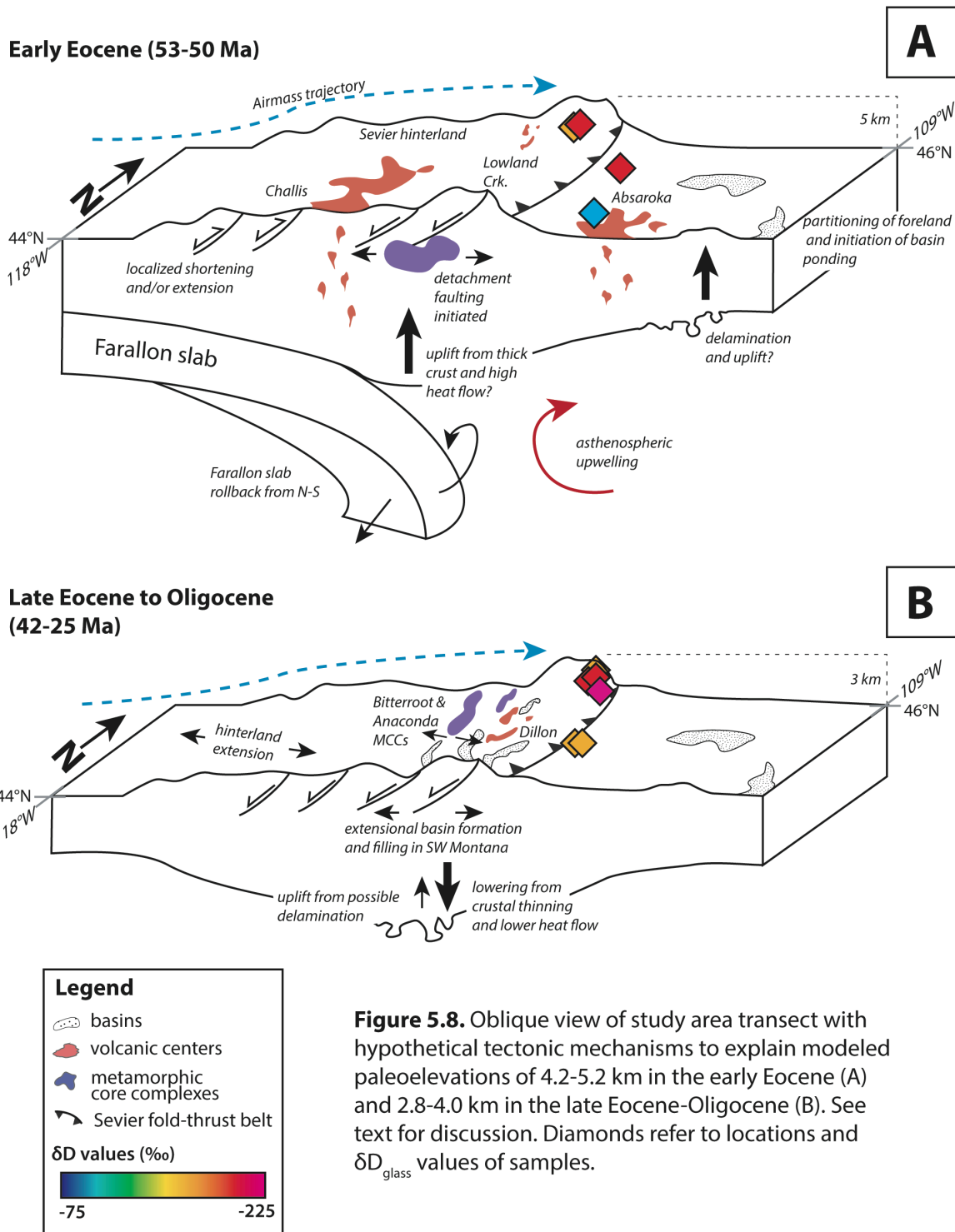**δD values (‰)**

-75   -225

Figure 5.8. Oblique view of study area transect with hypothetical tectonic mechanisms to explain modeled paleoelevations of 4.2-5.2 km in the early Eocene (A) and 2.8-4.0 km in the late Eocene-Oligocene (B). See text for discussion. Diamonds refer to locations and δD_{glass} values of samples.

In sum, high early Eocene paleoelevations of 4.2 – 5.2 km at the toe of the Sevier fold-thrust belt in west-central and southwest Montana are most likely the result of crustal thickening and the thermal uplift related to Farallon slab rollback (Fig. 5.8). Thick crust (50-55 km) created during the Cretaceous to Paleocene or early Eocene time supported 1.9 to 2.8 km of high topography, while the remaining Eocene surface uplift can be attributed to regional extension, high heat flow from volcanic activity and crustal hydration, and delamination of dense lithosphere contemporaneous with the north to south removal of the Farallon slab.

5.4.3. Surface Lowering After the Early Eocene

These new paleoelevation data show that, between the early Eocene and middle Eocene, southwestern and west-central Montana experienced surface lowering of between 200 and 2400 m to elevations of 2.8 – 4.0 km. Early Eocene samples in the region are dated to between 51 and 53.1 Ma, but samples taken from the Muddy Creek and Sage Creek Basins of comparable paleoelevation estimates are ca. 47-43 Ma, meaning that substantial surface lowering of this magnitude of may have taken place within as little as 4 Ma. Two other processes were taking place in the area at this time: waning volcanic activity and active extension (Yonkee and Weil, 2015). Based on palinspastic reconstructions of Coney and Harms (1984), the toe of the Sevier fold-thrust belt experienced 10-15 km of crustal thinning (β = 1.35) from the early Eocene for a modern crustal thickness of ~37 km (Gilbert, 2012). Crustal thicknesses predating Basin and Range extension are ~45 km (Coney and Harms, 1984). Using this value, ~1.4 km, or 35-50%, of regional high topography could be supported by thick crust, with the difference coming from other mechanisms, including delamination and removal of dense mineral phases (Fig. 5.8; Jones et al., 2015) (see section 5.4.1 for discussion of these mechanisms). The contemporaneous timing of surface lowering with decreased heat flow and with MCC extension and formation of the series of southwestern Montana basins like the Muddy Creek and Sage Creek must be considered when assessing drivers of surface lowering. With more detailed estimates of timing of extension, combined with paleoelevation estimates, future researchers could more easily characterize and track the progress of surface lowering.

6. CONCLUSIONS

1. In the Paleogene, the highest elevations of the U.S. Cordillera were located in central and southwest Montana from 53 Ma – 50 Ma.

2. Peak paleoelevations in central Montana during the early Eocene reached altitudes of 4,640 $^{+720}/_{-440}$ m, and _____ during the late Eocene, based on thermodynamic Rayleigh distillation modeling of $\Delta\delta D_{glass}$ values. Estimates of regional high topography here provide constraints that U.S. Cordilleran Paleogene tectonic and paleoclimate models must meet going forward.

3. Eocene east-central Idaho reached 3-3.5 km of elevation, in agreement with paleobotanical paleoaltimetry studies, but was not the regional paleo-high as previously thought.

4. To the east of the fold-thrust belt, airmass mixing and/or evaporative conditions resulted in increased δD_{glass} values.

5. High paleoelevations of 4.2 – 5.2 km in central Montana cannot be supported by isostatic compensation of thickened crust alone; they likely require additional support through thermal processes or delamination.

6. The effects of Farallon slab rollback, including crustal hydration, magmatism, and delamination fits with paleoelevation estimates and spatiotemporal patterns of volcanism and the locations of high elevations.

7. Based on geochemical correlations, Challis volcanic material traveled to the Wind River Basin and Green River Basin via air and/or ground transport.

8. Additional work is needed to quantify surface deformation in the western Great Plains region. Future studies would also benefit from refined timing of MCC exhumation to better constrain the timing of initiation of extension in western Montana.

7. REFERENCES

Acker, J.G. and Leptoukh, G., 2007, Online Analysis Enhances Use of NASA Earth Science Data, Eos, Trans. AGU, v. 88.

Anagnostou, E., John, E.H., Edgar, K.M., Foster, G.L., Ridgwell, A., Inglis, G.N., Pancost, R.D., Lunt, D.J., and Pearson, P.N., 2016, Changing atmospheric CO2 concentration was the primary driver of early Cenozoic climate: Nature, v. 533, p. 380–384, doi:10.1038/nature17423.

Axelrod, D., 1965, A Method for Determining the Altitudes of Tertiary Floras: Paleobotanist, p. 28.

Bershaw, J., Cassel, E.J., Carlson, T.B., Streig, A.R., and Streck, M.J., 2019, Volcanic glass as a proxy for Cenozoic elevation and climate in the Cascade Mountains, Oregon, USA: Journal of Volcanology and Geothermal Research, v. 381, p. 157–167, doi:10.1016/j.jvolgeores.2019.05.021.

Bershaw, J., Hansen, D.D., and Schauer, A.J., 2020, Deuterium excess and [17] O-excess variability in meteoric water across the Pacific Northwest, USA: Tellus B: Chemical and Physical Meteorology, v. 72, p. 1–17, doi:10.1080/16000889.2020.1773722.

Bestland, E.A., Hammond, P.E., Blackwell, D.L.S., Kays, M.A., Retallack, G.J., and Stimac, J. Geologic Framework of the Clarno Unit, John Day Fossil Beds National Monument, Central Oregon: , p. 40.

Bestland, E.A., and Retallack, G.J., 1994, Geology and Paleoenvironments of the Clarno Unit: , p. 241.

Blankenau, J.J., 1999, Cenozoic Structural and Stratigraphic Evolution of the Southeastern Salmon Basin, East- Central Idaho [M.S. thesis]: Logan, Utah, Utah State University, 113 p.

Brown, E., 2017, Rhyolite Petrogenesis at Tower Mountain Caldera, OR [M.S. thesis]: Portland, Portland State University, 312 p., doi:10.15760/etd.5881.

Canada, A.S., Cassel, E.J., Stockli, D.F., Smith, M.E., Jicha, B.R., and Singer, B.S., 2020, Accelerating exhumation in the Eocene North American Cordilleran hinterland: Implications from detrital zircon (U-Th)/(He-Pb) double dating: GSA Bulletin, v. 132, p. 198–214, doi:10.1130/B35160.1.

Canavan, R.R., Carrapa, B., Clementz, M.T., Quade, J., DeCelles, P.G., and Schoenbohm, L.M., 2014, Early Cenozoic uplift of the Puna Plateau, Central Andes, based on stable isotope paleoaltimetry of hydrated volcanic glass: Geology, v. 42, p. 447–450, doi:10.1130/G35239.1.

Carroll, A.R., Doebbert, A.C., Booth, A.L., Chamberlain, C.P., Rhodes-Carson, M.K., Smith, M.E., Johnson, C.M., and Beard, B.L., 2010, Capture of high-altitude precipitation by a low-altitude Eocene lake, western U.S.: Geology, v. 36, p. 761-764, doi: 10.1130/G24783A.1.

Cassel, E.J., and Breecker, D.O., 2017, Long-term stability of hydrogen isotope ratios in hydrated volcanic glass: Geochimica et Cosmochimica Acta, v. 200, p. 67–86, doi:10.1016/j.gca.2016.12.001.

Cassel, E.J., Breecker, D.O., Henry, C.D., Larson, T.E., and Stockli, D.F., 2014, Profile of a paleo-orogen: High topography across the present-day Basin and Range from 40 to 23 Ma: Geology, v. 42, p. 1007–1010, doi:10.1130/G35924.1.

Cassel E. J., Calvert A. T. and Graham S. A. (2009) Age, geochemical composition, and distribution of Oligocene ignimbrites in the northern Sierra Nevada, California: implications for landscape morphology, elevation, and drainage divide geography of the Nevadaplano: International Geology Review, v. 51, 723–742.

Cassel, E.J., Graham, S.A., Chamberlain, C.P., and Henry, C.D., 2012, Early Cenozoic topography, morphology, and tectonics of the northern Sierra Nevada and western Basin and Range: Geosphere, v. 8, p. 229–249, doi:10.1130/GES00671.1.

Cassel, E.J., Smith, M.E., and Jicha, B.R., 2018, The Impact of Slab Rollback on Earth's Surface: Uplift and Extension in the Hinterland of the North American Cordillera: Geophysical Research Letters, v. 45, doi:10.1029/2018GL079887.

Chamberlain, C.P., Mix, H.T., Mulch, A., Hren, M.T., Kent-Corson, M.L., Davis, S.J., Horton, T.W., and Graham, S.A., 2012, The Cenozoic climatic and topographic evolution of the western North American Cordillera: American Journal of Science, v. 312, p. 213–262, doi:10.2475/02.2012.05.

Chamberlain, C.P., and Poage, M.A., 2000, Reconstructing the paleotopography of mountain belts from the isotopic composition of authigenic minerals: Geology, v. 28, p. 115-118.

Chetel, L.M., Janecke, S.U., Carroll, A.R., Beard, B.L., Johnson, C.M., and Singer, B.S., 2011, Paleogeographic reconstruction of the Eocene Idaho River, North American Cordillera: Geological Society of America Bulletin, v. 123, p. 71–88, doi:10.1130/B30213.1.

Clayton, L., Moran, S.R., Bluemle, J.P., and Carlson, C.G., 1980, Geologic Map of North Dakota: U.S. Geological Survey.

Coney, P.J. & Harms, T.A., 1984. Cordilleran metamorphic core complexes: Cenozoic extensional relics of Mesozoic compression: Geology, v. 12, p. 550-554.

Constenius, K.N., 1996, Late Paleogene extensional collapse of the Cordilleran foreland fold and thrust belt: Geological Society of America Bulletin, p. 20.

DeCelles, P.G., 2004, Late Jurassic to Eocene evolution of the Cordilleran thrust belt and foreland basin system, western U.S.A.: American Journal of Science, v. 304, p. 105–168, doi:10.2475/ajs.304.2.105.

Dickinson, W.R., Klute, M.A., Hayes, M.J., Janecke, S.U., Lundin, E.R., McKittrick, M.A., Olivares, M.D., 1988, Paleogeographic and paleotectonic setting of Laramide sedimentary basins in the central Rocky Mountain region: Geological Society of America Bulletin, v. 100, p. 1023–1039.

Dickinson, W.R., 2004, Evolution of the North American Cordillera: Annual Review of Earth and Planetary Sciences, v. 32, p. 13–45, doi:10.1146/annurev.earth.32.101802.120257.

Druschke, P., Hanson, A.D., Wells, M.L., Rasbury, T., Stockli, D.F., and Gehrels, G., 2009, Synconvergent surface-breaking normal faults of Late Cretaceous age within the Sevier hinterland, east-central Nevada: Geology, v. 37, p. 447–450, doi:10.1130/G25546A.1.

Dudás, F.Ö., Ispolatov, V.O., Harlan, S.S., and Snee, L.W., 2010, ^{40}Ar/^{39}Ar Geochronology and Geochemical Reconnaissance of the Eocene Lowland Creek Volcanic Field, West-Central Montana: The Journal of Geology, v. 118, p. 295–304, doi:10.1086/651523.

Dumitru, T.A., Ernst, W.G., Wright, J.E., Wooden, J.L., Wells, R.E., Farmer, L.P., Kent, A.J.R., and Graham, S.A., 2013, Eocene extension in Idaho generated massive

sediment floods into the Franciscan trench and into the Tyee, Great Valley, and Green River basins: Geology, v. 41, p. 187–190, doi:10.1130/G33746.1.

Dunn, R., 2007, Climatically induced floral change across the Eocene-Oligocene transition in the John Day and Clarno Formations of eastern Oregon: Geological Society of America Abstracts with Programs, v. 39, no. 6, p. 567.

Fahrenbach, M.D., and Sawyer, J.F., 2011, Geologic Map of the Lemmon 1° x 2° Quadrangle, South Dakota and North Dakota: South Dakota Geological Survey 1° x 2° Series Geologic Quadrangle Map.

Fan, M., and Carrapa, B., 2014, Late Cretaceous-early Eocene Laramide uplift, exhumation, and basin subsidence in Wyoming: Crustal responses to flat slab subduction: Laramide uplift and exhumation: Tectonics, v. 33, p. 509–529, doi:10.1002/2012TC003221.

Fan, M., Constenius, K.N., Phillips, R.F., and Dettman, D.L., 2021, Late Paleogene paleotopographic evolution of the northern Cordilleran orogenic front: Implications for demise of the orogen: Geological Society of America Bulletin, 18 p. doi:10.1130/B35919.1.

Fan, M., Heller, P., Allen, S.D., and Hough, B.G., 2014a, Middle Cenozoic uplift and concomitant drying in the central Rocky Mountains and adjacent Great Plains: Geology, v. 42, p. 547–550, doi:10.1130/G35444.1.

Fan, M., Hough, B.G., and Passey, B.H., 2014b, Middle to late Cenozoic cooling and high topography in the central Rocky Mountains: Constraints from clumped isotope geochemistry: Earth and Planetary Science Letters, v. 408, p. 35–47, doi:10.1016/j.epsl.2014.09.050.

Feng, R., and Poulsen, C.J., 2016, Refinement of Eocene lapse rates, fossil-leaf altimetry, and North American Cordilleran surface elevation estimates: Earth and Planetary Science Letters, v. 436, p. 130–141, doi:10.1016/j.epsl.2015.12.022.

Feng, R., Poulsen, C.J., Werner, M., Chamberlain, C.P., Mix, H.T., and Mulch, A., 2013, Early Cenozoic evolution of topography, climate, and stable isotopes in precipitation in the North American Cordillera: American Journal of Science, v. 313, p. 613–648, doi:10.2475/07.2013.01.

Ferreira, G., 2000, Arsenic Mobilization from Silicic Volcanic Rocks in the Southern Willamette Valley [M.S. thesis]: Portland, Portland State University, 102 p. doi:10.15760/etd.2753.

Foster, D.A., Grice, W.C., and Kalakay, T.J., 2010, Extension of the Anaconda metamorphic core complex: 40Ar/39Ar thermochronology and implications for Eocene tectonics of the northern Rocky Mountains and the Boulder batholith: Lithosphere, v. 2, p. 232–246, doi:10.1130/L94.1.

Freeman, V.L., Ruppel, E.T., and Klepper, M.R., 1958, Geology of part of the Townsend Valley, Broadwater and Jefferson Counties, Montana: U.S. Geological Survey Bulletin 1042-N, p. 481‑ 556.

Fritz, W.J., Sears, J.W., McDowell, R.J., and Wampler, J.M., 2007, Cenozoic volcanic rocks of southwestern Montana: Northwest Geology, v. 36, p. 91–110.

Galewsky, J., 2009, Orographic precipitation isotopic ratios in stratified atmospheric flows: Implications for paleoelevation studies: Geology, v. 37, p. 791–794, doi:10.1130/G30008A.1.

Gin, S., Ryan, J.V., Schreiber, D.K., Neeway, J., and Cabié, M., 2013, Contribution of atom-probe tomography to a better understanding of glass alteration mechanisms: Application to a nuclear glass specimen altered 25 years in a granitic environment: Chemical Geology, v. 349, p. 99-109.

Gin, S., Jollivet, P., Fournier, M., Angeli, F., Frugier, P., and Charpentier, T., 2015, Origin and consequences of silicate glass passivation by surface layers: Nature Communications, v. 6, p. 6360, doi:10.1038/ncomms7360.

Harlan, S.S., 2006, 40Ar/39Ar dates from alkaline intrusions in the northern Crazy Mountains, Montana: Implications for the timing and duration of alkaline magmatism in the central Montana alkalic province: Rocky Mountain Geology, v. 41, p. 45–55, doi:10.2113/gsrocky.41.1.45.

Hausel, W.D., 1996, Geology and gold mineralization of the Rattlesnake Hills, Granite Mountains, Wyoming: Wyoming State Geological Survey 52, 36 p.

Heller, P.L., Dueker, K., and McMillan, M.E., 2003, Post-Paleozoic alluvial gravel transport as evidence of continental tilting in the U.S. Cordillera: Geological Society of America Bulletin, v. 115, p. 1122–1132, doi:10.1130/B25219.1.

Heller, P.L., and Liu, L., 2016, Dynamic topography and vertical motion of the U.S. Rocky Mountain region prior to and during the Laramide orogeny: Geological Society of America Bulletin, v. 128, p. 973–988, doi:10.1130/B31431.1.

Hildreth, W. and Mahood, G., 1985, Correlation of ash-flow tuffs: Geological Society of American Bulletin, v. 96, p. 968-974.

Hiza, M.M., 1999, The Geochemistry and Geochronology of the Eocene Absaroka Volcanic Province, Northern Wyoming and Southwest Montana, USA [Ph.D. thesis]: Oregon State University, 243 p.

Hoefs J., 1997, Stable Isotope Geochemistry, 4th. ed.: Springer-Verlag, 201 p.

Huber, M., Caballero, R., 2011, The early Eocene equable climate problem revisited: Climate of the Past, v. 7, p. 603–633.

Kent-Corson, M.L., Sherman, L.S., Mulch, A., and Chamberlain, C.P., 2006, Cenozoic topographic and climatic response to changing tectonic boundary conditions in Western North America: Earth and Planetary Science Letters, v. 252, p. 453–466, doi:10.1016/j.epsl.2006.09.049.

Humphreys, E., Hessler, E., Dueker, K., Farmer, G.L., Erslev, E., Atwater, T., 2003, How Laramide-age hydration of North American lithosphere by the Farallon slab controlled subsequent activity in the western United States: International Geology Review, v. 45, p. 575–595.

Humphreys, E., 2009, Relation of flat subduction to magmatism and deformation in the western United States, *in* Backbone of the Americas: Shallow Subduction, Plateau Uplift, and Ridge and Terrane Collision, Geological Society of America, doi:10.1130/2009.1204(04).

Humphreys, E.D., Schmandt, B., Bezada, M.J., and Perry-Houts, J., 2015, Recent craton growth by slab stacking beneath Wyoming: Earth and Planetary Science Letters, v. 429, p. 170–180, doi:10.1016/j.epsl.2015.07.066.

Hyndman, R.D., 2015, Tectonic Consequences of a Uniformly Hot Backarc and Why is the Cordilleran Mountain Belt High?: Geoscience Canada, v. 42, p. 383-402, doi:10.12789/geocanj.2015.42.078.

IAEA/WMO (2021). Global Network of Isotopes in Precipitation. The GNIP Database. Accessible at: https://nucleus.iaea.org/wiser

Janecke, S.U., & Snee, L.W., 1993, Timing and episodicity of middle Eocene Volcanism and onset of conglomerate formation, Idaho: Journal of Geology, v. 101, p. 603-621. doi: 10.1086/648252.

Janecke, S.U., 1994, Sedimentation and paleogeography of an Eocene to Oligocene rift zone, Idaho and Montana: Geological Society of America Bulletin, v. 106, p. 1083-1095.

Janecke, S.U., McIntosh, W., & Good, S., 1999, Testing models of rift basins: structure and stratigraphy of an Eocene-Oligocene supradetachment basin, Muddy Creek half graben, south-west Montana: Basin Research, v. 11, p. 143-165.

Janecke, S.U., VanDenburg, C.J., Blankenau, J.J., & M'Gonigle, J.W., 2000, Long-distance longitudinal transport of gravel across the Cordilleran thrust belt of Montana and Idaho: Geology, v. 28, p. 439-442.

Jones, C.H., Mahan, K.H., Butcher, L.A., Levandowski, W.B., and Farmer, G.L., 2015, Continental uplift through crustal hydration: Geology, v. 43, p. 355–358, doi:10.1130/G36509.1.

Karlstrom, K.E. et al., 2012, Mantle-driven dynamic uplift of the Rocky Mountains and Colorado Plateau and its surface response: Toward a unified hypothesis: Lithosphere, v. 4, p. 3–22, doi:10.1130/L150.1.

Kendall, C., and Coplen, T.B., 2001, Distribution of oxygen-18 and deuterium in river waters across the United States: Hydrological Processes, v. 15, p. 1363–1393, doi:10.1002/hyp.217.

Kohn, M.J., Miselis, J.L., and Fremd, T.J., 2002, Oxygen isotope evidence for progressive uplift of the Cascade Range, Oregon: Earth and Planetary Science Letters, v. 204, p. 151–165, doi:10.1016/S0012-821X(02)00961-5.

Konstantinou, A., Strickland, A., Miller, E.L., and Wooden, J.P., 2012, Multistage Cenozoic extension of the Albion–Raft River–Grouse Creek metamorphic core complex: Geochronologic and stratigraphic constraints: Geosphere, v. 8, p. 1429–1466, doi:10.1130/GES00778.1.

Kukla, T., Ibarra, D.E., Rugenstein, J.K.C., Gooley, J.T., Mullins, C.E., Kramer, S., Moragne, D.Y., and Chamberlain, C.P., 2021, High-Resolution Stable Isotope Paleotopography of the John Day Region, Oregon, United States: Frontiers in Earth Science, v. 9, p. 635181, doi:10.3389/feart.2021.635181.

Larson, E.E., and Evanoff, E., 1998, Tephrostratigraphy and source of the tuffs of the White River sequence, *in* Depositional Environments, Lithostratigraphy, and Biostratigraphy of the White River and Arikaree Groups (Late Eocene to Early Miocene, North America), Geological Society of America Special Paper 325, 14 p., doi:10.1130/0-8137-2325-6.1.

Levandowski, W., Jones, C.H., Butcher, L.A., and Mahan, K.H., 2018, Lithospheric density models reveal evidence for Cenozoic uplift of the Colorado Plateau and Great Plains by lower-crustal hydration: Geosphere, v. 14, p. 1150–1164, doi:10.1130/GES01619.1.

Lisenbee, A.L., 1988, Tectonic History of the Black Hills Uplift, *in* Thirty-Ninth Field Conference Guidebook, Eastern Powder River Basin - Black Hills., Casper, Wyoming, Wyoming Geological Association, p. 45-52.

Li, L., and Fan, M., 2018, Cenozoic Sediment Provenance in the Northern Great Plains Corresponds to Four Episodes of Tectonic and Magmatic Events in the Central North American Cordillera: Tectonics, v. 37, p. 4018–4036, doi:10.1029/2018TC005213.

McClaughry, J.D., 2009, Preliminary Geologic Map of the Sweet Home 7.5' Quadrangle, Linn Country, Oregon: Oregon Department of Geology and Mineral Industries Open File Report O-09-11, scale 1:24,000, 1 sheet.

McClaughry, J.D., Wiley, T.J., Ferns, M.L., and Madin, I.P., 2010, Geology of the Southern Willamette Valley: Oregon Department of Geology and Mineral Industries Open File Report O-10-03, scale 1:63,360, 1 sheet.

McDonald, C., Mosolf, J.G., Vuke, S.M., and Lonn, J.D., 2020, Geologic Map of the Elliston 30′ x 60′ Quadrangle, West-Central Montana, Montana Bureau of Mines and Geology Geologic Map 77, scale: 1:250,000, 40 p.

McDonough, W.F. and Sun, S.S., 1995, The composition of the Earth: Chemical Geology, v. 120, p. 223-253.

McMillan, M.E., Heller, P.L., and Wing, S.L., 2006, History and causes of post-Laramide relief in the Rocky Mountain orogenic plateau: Geological Society of America Bulletin, v. 118, p. 393–405, doi:10.1130/B25712.1.

M'Gonigle, J.W., and Dalrymple, G.B., 1996, 40Ar/39Ar ages of some Challis Volcanic Group rocks and the initiation of Tertiary sedimentary basins in southwestern

Montana: United States Geological Survey U.S. Geological Survey Bulletin 2132, 26 p., doi:10.3133/b2132.

Mix, H.T., Mulch, A., Kent-Corson, M.L., and Chamberlain, C.P., 2011, Cenozoic migration of topography in the North American Cordillera: Geology, v. 39, p. 87–90, doi:10.1130/G31450.1.

Mulch, A., 2016, Stable isotope paleoaltimetry and the evolution of landscapes and life: Earth and Planetary Science Letters, v. 433, p. 180–191, doi:10.1016/j.epsl.2015.10.034.

Mulch, A., Teyssier, C., Cosca, M.A., and Chamberlain, C.P., 2007, Stable isotope paleoaltimetry of Eocene core complexes in the North American Cordillera: Core Complex Paleoaltimetry: Tectonics, v. 26, 13 p., doi:10.1029/2006TC001995.

Mulch, A., Teyssier, C., Cosca, M.A., Vanderhaeghe, O., and Vennemann, T.W., 2004, Reconstructing paleoelevation in eroded orogens: Geology, v. 32, p. 525, doi:10.1130/G20394.1.

Poage, M.A., and Chamberlain, C.P., 2001, Empirical relationships between elevation and the stable isotope composition of precipitation and surface waters: considerations for studies of paleoelevation change: American Journal of Science, v. 301, p. 1–15, doi:10.2475/ajs.301.1.1.

Porter, R., Liu, Y., and Holt, W.E., 2016, Lithospheric records of orogeny within the continental U.S.: Geophysical Research Letters, v. 43, p. 144–153, doi:10.1002/2015GL066950.

Poulsen, C.J., and Jeffery, M.L., 2011, Climate change imprinting on stable isotopic compositions of high-elevation meteoric water cloaks past surface elevations of major orogens: Geology, v. 39, p. 595–598, doi:10.1130/G32052.1.

Redden, J.A., DeWitt, E., Geological Survey (U.S.), and South Dakota School of Mines and Technology Foundation, 2008, Maps showing geology structure and geophysics of the central Black Hills South Dakota: U.S. Geological Survey.

Retallack, G.J., Orr, W.N., Prothero, D.R., Duncan, R.A., Kester, P.R., and Ambers, C.P., 2004, Eocene-Oligocene extinction and paleoclimatic change near Eugene, Oregon: Geological Society of America Bulletin, v. 116, p. 817, doi:10.1130/B25281.1.

Rey, P., Vanderhaeghe, O., and Teyssier, C., 2001, Gravitational collapse of the continental crust: definition, regimes and modes: Tectonophysics, v. 342, p. 435–449, doi:10.1016/S0040-1951(01)00174-3.

Rowley, D.B., 2007, Stable Isotope-Based Paleoaltimetry: Theory and Validation: Reviews in Mineralogy and Geochemistry, v. 66, p. 23–52, doi:10.2138/rmg.2007.66.2.

Rowley, D.B., and Garzione, C.N., 2007, Stable Isotope-Based Paleoaltimetry: Annual Review of Earth and Planetary Sciences, v. 35, p. 463–508, doi:10.1146/annurev.earth.35.031306.140155.

Rowley, D.B., Pierrehumbert, R.T., and Currie, B.S., 2001, A new approach to stable isotope-based paleoaltimetry: implications for paleoaltimetry and paleohypsometry of the High Himalaya since the Late Miocene: Earth and Planetary Science Letters, v. 188, p. 253–268, doi:10.1016/S0012-821X(01)00324-7.

Sanford, R.F., 2005, Geology and stratigraphy of the Challis Volcanic Group and related rocks, Little Wood River area, south-central Idaho, with a section on Geochronology by Lawrence W. Snee: U.S. Geological Survey Bulletin 2064-II, 22 p., doi:10.3133/sir20165089E.

Savoie, C., 2000, Arsenic Mobility and Compositional Variability in High-Silica Ash Flow Tuffs [M.S. thesis]: Portland, Portland State University, 154 p., doi:10.15760/etd.1012.

Scarberry, K.C., Yakovlev, P.V., and Schwartz, T.M. Mesozoic Magmatism in Montana: Montana Bureau of Mines and Geology, 30 p.

Schwartz, T.M., Methner, K., Mulch, A., Graham, S.A., and Chamberlain, C.P., 2019, Paleogene topographic and climatic evolution of the Northern Rocky Mountains from integrated sedimentary and isotopic data: GSA Bulletin, v. 131, p. 1203–1223, doi:10.1130/B32068.1.

Sharp, Z.D., 2017, Principles of Stable Isotope Geochemistry: 385 p.

Sheriff, S.D., and Shive, P.N., 1980, The Rattlesnake Hills of central Wyoming revisited: Further paleomagnetic results: Geophysical Research Letters, v. 7, p. 589–592, doi:10.1029/GL007i008p00589.

Smedes, W. H. and Prostka, H. J., 1972, Stratigraphic framework of the Absaroka Volcanic Supergroup in Yellowstone National Park region: U.S. Geological Survey Professional Paper 729-C, 33 p.

Smith, M.E., Carroll, A.R., Jicha, B.R., Cassel, E.J., and Scott, J.J., 2014, Paleogeographic record of Eocene Farallon slab rollback beneath western North America: Geology, v. 42, p. 1039–1042, doi:10.1130/G36025.1.

Smith, M.E., Carroll, A.R., and Singer, B.S., 2008, Synoptic reconstruction of a major ancient lake system: Eocene Green River Formation, western United States: Geological Society of America Bulletin, v. 120, p. 54–84, doi:10.1130/B26073.1.

Smith, M.E., Cassel, E.J., Jicha, B.R., Singer, B.S., and Canada, A.S., 2017, Hinterland drainage closure and lake formation in response to middle Eocene Farallon slab removal, Nevada, U.S.A.: Earth and Planetary Science Letters, v. 479, p. 156–169, doi:10.1016/j.epsl.2017.09.023.

Snell, K.E., Koch, P.L., Druschke, P., Foreman, B.Z., and Eiler, J.M., 2014, High elevation of the 'Nevadaplano' during the Late Cretaceous: Earth and Planetary Science Letters, v. 386, p. 52–63, doi:10.1016/j.epsl.2013.10.046.

Sonder, L.J., and Jones, C.H., 1999, Western United States Extension: How the West was Widened: Annual Review of Earth and Planetary Sciences, v. 27, p. 417–462, doi:10.1146/annurev.earth.27.1.417.

Stroup, C.N., Link, P.K., Janecke, S.U., Fanning, C.M., Yaxley, G.M., and Beranek, L.P., 2008, Eocene to Oligocene provenance and drainage in extensional basins of southwest Montana and east-central Idaho: Evidence from detrital zircon populations in the Renova Formation and equiva- lent strata: Arizona Geological Society Digest 22, p. 529–546.

Tabrum, A.R., and Nichols, R., 2001, Tertiary paleontology of southwest Montana and adjacent Idaho, *in* Nichols, R., ed., Cenozoic vertebrate paleontology and geology of southwestern Montana and adjacent areas, *in* Hill, C.L., ed., Mesozoic and Cenozoic paleontology in the western plains and Rocky Mountains: Society of Vertebrate Paleontology 61st annual field trip guidebook, Museum of the Rockies Occasional Paper no. 3, p. 88–112.

Thoning, K.W., Crotwell, A.M., and Mund, J.W. (2021), Atmospheric Carbon Dioxide Dry Air Mole Fractions from continuous measurements at Mauna Loa, Hawaii, Barrow, Alaska, American Samoa and South Pole. 1973-2019, Version 2021-02 National Oceanic and Atmospheric Administration (NOAA), Global Monitoring Laboratory (GML), Boulder, Colorado, USA. https://doi.org/10.15138/yaf1-bk21

Thoresen, H.E., and Cassel, E.J., 2020, Eocene Basin Record of Metamorphic Core Complex Exhumation in the Western United State Cordillera, Geological Society of America Abstracts with Program, v. 52.

Tsukui, K., 2016, Chronology and Faunal Evolution of the Middle Eocene Bridgerian North American Land Mammal "Age": Achieving High Precision Geochronology (PhD dissertation]: New York, Columbia University, 272 p.

Vachon, R.W., Welker, J.M., White, J.W.C., and Vaughn, B.H., 2010, Monthly precipitation isoscapes (δ^{18}O) of the United States: Connections with surface temperatures, moisture source conditions, and air mass trajectories: Journal of Geophysical Research, v. 115, p. D21126, doi:10.1029/2010JD014105.

Vachon, R.W., White, J.W.C., Gutmann, E., and Welker, J.M., 2007, Amount-weighted annual isotopic (δ^{18}O) values are affected by the seasonality of precipitation: A sensitivity study: Geophysical Research Letters, v. 34, p. L21707, doi:10.1029/2007GL030547.

van der Ent, R.J., Wang-Erlandsson, L., Keys, P.W., and Savenije, H.H.G., 2014, Contrasting roles of interception and transpiration in the hydrological cycle – Part 2: Moisture recycling: Earth System Dynamics, v. 5, p. 471–489, doi:10.5194/esd-5-471-2014.

VanHouten, F. B., 1964, Tertiary geology of the Beaver Rim area, Fremont and Natrona Counties, Wyoming: U.S. Geol. Survey Bull. 1164, 99 p.

Vuke, S.M., 2003, Geology of western and northern Gallatin Valley, southwestern Montana: Montana Bureau of Mines and Geology Open-File Report 481, 40 p., 1 sheet, scale 1:50,000.

Vuke, S.M., 2007, Geologic Map of Radersburg-Toston Basin, Montana, southwestern Montana: Montana Bureau of Mines and Geology Open-File Report 561, 18 p., 1 sheet, scale 1:50,000, 18 p.

Vuke, S.M., 2011, Geologic Map of the Canyon Ferry Lake area, West Central Montana: Montana Bureau of Mines and Geology Open-File Report 607, 18 p., 1 sheet, scale 1:50,000.

Waterisotopes Database (2020) http://waterisotopesDB.org. Accessed 12/15/2020. Query: Country=USA, Type=Precipitation; River.

Wells, M.L., Hoisch, T.D., Cruz-Uribe, A.M., and Vervoort, J.D., 2012, Geodynamics of synconvergent extension and tectonic mode switching: Constraints from the Sevier-Laramide orogen: TECTONIC MODE SWITCHING, SEVIER OROGEN: Tectonics, v. 31, p. n/a-n/a, doi:10.1029/2011TC002913.

Wilson, A.B., Hayes, T.S., Benson, M.E., Yager, D.B., Anderson, E.D., Bleiwas, D.I., DeAngelo, J., Dicken, C.L., Drake, R.M., II, Fernette, G.L., Giles, S.A., Glen, J.M.G., Haacke, J.E., Horton, J.D., Parks, H.L., Rockwell, B.W., and Williams, C.F., 2016, Geology and mineral resources of the Southwestern and South-Central Wyoming Sagebrush Focal Area, Wyoming, and the Bear River Watershed Sagebrush Focal Area, Wyoming and Utah, (ver. 1.1, October 26, 2016): U.S. Geological Survey Scientific Investigations Report 2016–5089–E, 128 p., http://dx.doi.org/10.3133/sir20165089E.

Wolfe, J.A., Gregory-Wodzicki, K.M., Molnar, P., and Mustoe, G., 2000, Paleobotanical evidence for the development of high altitudes during the early Eocene in northwestern North America: GFF, v. 122, p. 186–187, doi:10.1080/11035890001221186.

Yang, J., Spicer, R.A., Spicer, T.E.V., and Li, C.-S., 2011, 'CLAMP Online': a new web-based palaeoclimate tool and its application to the terrestrial Paleogene and Neogene of North America: Palaeobiodiversity and Palaeoenvironments, v. 91, p. 163–183, doi:10.1007/s12549-011-0056-2.

Yonkee, W.A., and Weil, A.B., 2015, Tectonic evolution of the Sevier and Laramide belts within the North American Cordillera orogenic system: Earth-Science Reviews, v. 150, p. 531–593, doi:10.1016/j.earscirev.2015.08.001.

Zachos, J.C., Stott, L.D., and Lohmann, K.C., 1994, Evolution of Early Cenozoic marine temperatures: Paleoceanography, v. 9, p. 353–387, doi:10.1029/93PA03266.

Zachos, J., 2001, Trends, Rhythms, and Aberrations in Global Climate 65 Ma to Present: Science, v. 292, p. 686–693, doi:10.1126/science.1059412.

Zachos, J.C., Dickens, G.R., and Zeebe, R.E., 2008, An early Cenozoic perspective on greenhouse warming and carbon-cycle dynamics: Nature, v. 451, p. 279–283, doi:10.1038/nature06588.

Zhu, L., Fan, M., Hough, B., and Li, L., 2018, Spatiotemporal distribution of river water stable isotope compositions and variability of lapse rate in the central Rocky Mountains: Controlling factors and implications for paleoelevation reconstruction: Earth and Planetary Science Letters, v. 496, p. 215–226, doi:10.1016/j.epsl.2018.05.047.

Zhu, J., Poulsen, C.J., Otto-Bliesner, B.L., Liu, Z., Brady, E.C., and Noone, D.C., 2020, Simulation of early Eocene water isotopes using an Earth system model and its implication for past climate reconstruction: Earth and Planetary Science Letters, v. 537, p. 116164, doi:10.1016/j.epsl.2020.116164.

APPENDIX.

A1. Trace and Rare Earth Element Concentrations

Table A1. Trace and rare earth element concentrations (ppm) of analyzed samples.

	ND20_402SB-A	ND20_404SB-A	ND20_404SB-B	WU14_012ML	UT15_033DP	16OR_003JD
Sr	243	229	241	97	168	618
Rb	114.8	103.7	105.6	247.2	194.0	13.9
Ba	960	972	1149	577	720	4299
Th	9.64	10.20	10.30	27.42	36.31	6.46
Ta	0.71	0.73	0.73	1.30	1.59	1.98
Nb	7.24	7.51	7.43	11.64	13.17	10.63
Ce	42.20	43.39	44.48	53.20	71.61	38.41
Zr	69	69	70	72	89	155
Hf	2.39	2.46	2.56	2.73	3.15	4.67
Sm	2.46	2.54	2.64	2.46	2.09	4.18
Y	9.74	10.10	10.10	10.88	7.50	18.00
Yb	0.96	1.00	1.01	1.29	0.93	2.34
La	24.13	24.48	25.39	30.01	45.19	16.74
Ce	42.20	43.39	44.48	53.20	71.61	38.41
Pr	4.56	4.66	4.76	5.35	6.53	4.86
Nd	15.31	15.56	16.19	16.39	17.73	18.95
Sm	2.46	2.54	2.64	2.46	2.09	4.18
Eu	0.48	0.47	0.50	0.27	0.39	0.62
Gd	1.91	1.99	2.06	1.82	1.33	3.96
Tb	0.29	0.30	0.30	0.28	0.20	0.69
Dy	1.55	1.65	1.65	1.59	1.11	4.00
Ho	0.31	0.33	0.34	0.34	0.23	0.78
Er	0.89	0.93	0.95	1.04	0.71	2.10
Tm	0.14	0.15	0.16	0.18	0.13	0.35
Yb	0.96	1.00	1.01	1.29	0.93	2.34
Lu	0.15	0.16	0.17	0.23	0.16	0.37
Pb	23.38	24.00	24.39	36.87	34.41	3.99
Cs	5.40	5.58	5.59	12.58	7.04	0.39
Sc	2.1	1.9	2.0	0.9	1.3	0.7
U	5.21	5.43	5.50	11.04	9.14	1.77

	WU14_052WR-B	WU14_SCM-1	18WY_123SLT-D	WY19_338AB-B	WY19_345CP-B	WY20_444WB-A
Sr	3230	131	355	1351	124	582
Rb	21.2	189.5	46.8	49.2	23.6	60.8
Ba	5984	667	2218	5610	337	1974
Th	2.68	23.11	0.53	5.13	0.67	2.03
Ta	0.41	2.31	3.08	1.12	1.53	1.20
Nb	3.13	21.38	4.65	10.57	4.01	3.94
Ce	8.51	57.57	2.57	66.22	9.86	14.71
Zr	35	88	39	59	128	27
Hf	1.07	3.44	1.81	1.72	3.29	2.78
Sm	0.51	3.97	0.14	3.86	0.44	0.76
Y	2.32	20.76	0.50	13.38	0.64	1.78
Yb	0.26	2.05	0.13	1.35	0.07	0.21
La	4.69	31.76	1.51	38.47	5.94	9.05
Ce	8.51	57.57	2.57	66.22	9.86	14.71
Pr	0.90	6.15	0.26	6.90	1.00	1.50
Nd	3.04	20.35	0.86	23.31	3.27	4.88
Sm	0.51	3.97	0.14	3.86	0.44	0.76
Eu	0.26	0.42	0.21	0.92	0.20	0.43
Gd	0.42	3.54	0.09	3.09	0.27	0.49
Tb	0.06	0.58	0.01	0.46	0.03	0.06
Dy	0.35	3.44	0.08	2.56	0.14	0.33
Ho	0.08	0.69	0.02	0.52	0.02	0.06
Er	0.22	1.98	0.06	1.44	0.06	0.18
Tm	0.04	0.32	0.01	0.22	0.01	0.03
Yb	0.26	2.05	0.13	1.35	0.07	0.21
Lu	0.04	0.32	0.02	0.19	0.01	0.03
Pb	10.91	30.31	5.38	7.53	4.55	10.53
Cs	0.44	8.79	0.88	1.52	4.25	0.94
Sc	1.2	2.0	0.6	1.3	0.7	1.0
U	0.82	8.68	0.30	3.73	0.19	0.58

Table A1, cont'd.

	WY20_450WB-A	WY20_451WB-A	WY20_452WB-A	MT15_016CC	18MT_108LIVALN	18MT_114SC-B
Sr	95	118	71	47	31	88
Rb	139.7	189.4	213.3	243.8	114.0	135.0
Ba	528	380	310	154	922	906
Th	10.97	12.47	20.86	13.26	13.90	13.49
Ta	1.60	2.15	2.67	3.24	3.91	2.13
Nb	13.15	19.75	26.61	32.44	64.84	31.00
Ce	27.33	37.07	46.52	16.05	154.66	126.72
Zr	37	88	88	66	463	328
Hf	1.82	3.73	3.91	3.53	13.60	9.45
Sm	3.08	4.12	6.38	1.90	16.45	13.80
Y	22.36	39.49	47.70	15.45	101.85	83.91
Yb	2.03	3.68	4.25	1.54	10.10	8.17
La	14.08	18.97	21.67	8.17	73.74	54.56
Ce	27.33	37.07	46.52	16.05	154.66	126.72
Pr	3.25	4.29	5.84	2.08	19.10	14.80
Nd	11.97	15.79	22.60	7.72	75.41	59.59
Sm	3.08	4.12	6.38	1.90	16.45	13.80
Eu	0.48	0.61	0.56	0.32	2.24	1.95
Gd	3.24	4.92	7.16	1.95	16.93	14.32
Tb	0.58	0.97	1.30	0.34	2.93	2.44
Dy	3.49	6.21	7.90	2.04	17.86	14.83
Ho	0.73	1.31	1.61	0.44	3.75	3.10
Er	2.03	3.73	4.43	1.33	10.45	8.59
Tm	0.33	0.59	0.70	0.23	1.65	1.33
Yb	2.03	3.68	4.25	1.54	10.10	8.17
Lu	0.31	0.55	0.63	0.25	1.56	1.24
Pb	31.10	33.52	32.15	71.88	13.90	20.04
Cs	5.95	6.06	6.63	10.84	4.42	6.16
Sc	2.6	3.3	3.9	3.6	1.7	6.1
U	6.10	7.02	7.38	10.50	4.53	4.10

	18MT_112VC-B	18MT_129CR	MT19_344TF-A	MT20_426CF-B	MT20_426CF-A	MT20_424CF-B
Sr	148	215	183	138	139	159
Rb	115.5	164.9	61.3	78.4	76.6	148.3
Ba	772	983	896	683	687	796
Th	12.04	11.42	4.45	7.46	7.42	10.50
Ta	1.08	0.82	0.41	1.01	1.01	1.53
Nb	13.11	9.06	4.87	15.36	15.74	20.10
Ce	56.92	46.11	30.66	61.35	61.99	64.57
Zr	196	98	109	276	285	236
Hf	5.63	3.14	3.39	7.52	7.75	6.70
Sm	5.45	2.33	2.68	7.62	7.81	6.71
Y	30.87	7.34	16.24	46.90	48.24	42.21
Yb	3.11	0.70	1.88	4.89	4.91	4.25
La	29.54	27.07	15.45	28.38	28.56	31.45
Ce	56.92	46.11	30.66	61.35	61.99	64.57
Pr	6.92	4.77	3.68	8.10	8.14	7.78
Nd	25.85	14.99	13.66	32.87	33.70	29.97
Sm	5.45	2.33	2.68	7.62	7.81	6.71
Eu	0.85	0.42	0.47	1.64	1.68	1.05
Gd	5.20	1.60	2.47	8.09	8.22	6.77
Tb	0.86	0.22	0.40	1.35	1.38	1.16
Dy	5.13	1.19	2.46	8.20	8.35	7.04
Ho	1.07	0.24	0.53	1.73	1.76	1.48
Er	3.07	0.67	1.61	4.87	4.91	4.24
Tm	0.49	0.11	0.28	0.78	0.78	0.68
Yb	3.11	0.70	1.88	4.89	4.91	4.25
Lu	0.50	0.11	0.32	0.76	0.78	0.67
Pb	18.02	32.66	12.14	14.22	14.08	18.25
Cs	5.47	6.97	2.87	4.18	4.21	5.85
Sc	5.4	1.6	2.9	12.7	13.5	4.4
U	4.27	4.85	1.94	2.58	2.58	3.63

Table A1, cont'd.

	MT20_464MC-A	MT20_465MC-A	MT20_476CF-B	MT20_JEFF[0]	MT20_JEFF[9]
Sr	41	186	11	101	33
Rb	121.7	135.6	202.7	115.7	176.6
Ba	139	502	229	728	255
Th	7.31	8.90	33.00	13.61	21.30
Ta	1.71	2.57	3.81	0.90	1.53
Nb	9.70	18.50	58.39	10.75	19.45
Ce	21.19	50.94	204.99	50.72	56.07
Zr	50	57	313	202	110
Hf	1.76	1.92	10.25	5.99	3.96
Sm	1.12	2.58	14.62	4.50	4.61
Y	3.43	5.84	76.19	26.85	25.69
Yb	0.34	0.56	7.23	2.78	2.64
La	12.07	28.65	102.48	24.99	28.05
Ce	21.19	50.94	204.99	50.72	56.07
Pr	2.21	5.19	22.00	6.02	6.45
Nd	7.08	16.63	77.92	22.09	22.40
Sm	1.12	2.58	14.62	4.50	4.61
Eu	0.17	0.53	0.64	0.64	0.47
Gd	0.83	1.77	13.53	4.36	4.09
Tb	0.12	0.24	2.23	0.72	0.68
Dy	0.64	1.17	13.28	4.34	4.09
Ho	0.12	0.21	2.74	0.92	0.85
Er	0.32	0.54	7.68	2.71	2.48
Tm	0.05	0.08	1.20	0.43	0.41
Yb	0.34	0.56	7.23	2.78	2.64
Lu	0.05	0.08	1.11	0.44	0.42
Pb	4.78	6.27	32.23	19.46	24.16
Cs	2.35	1.74	3.54	7.41	6.88
Sc	1.3	2.1	1.6	4.6	3.4
U	1.89	2.12	7.71	4.95	7.41

A2. Modern Water Charts and Calculations

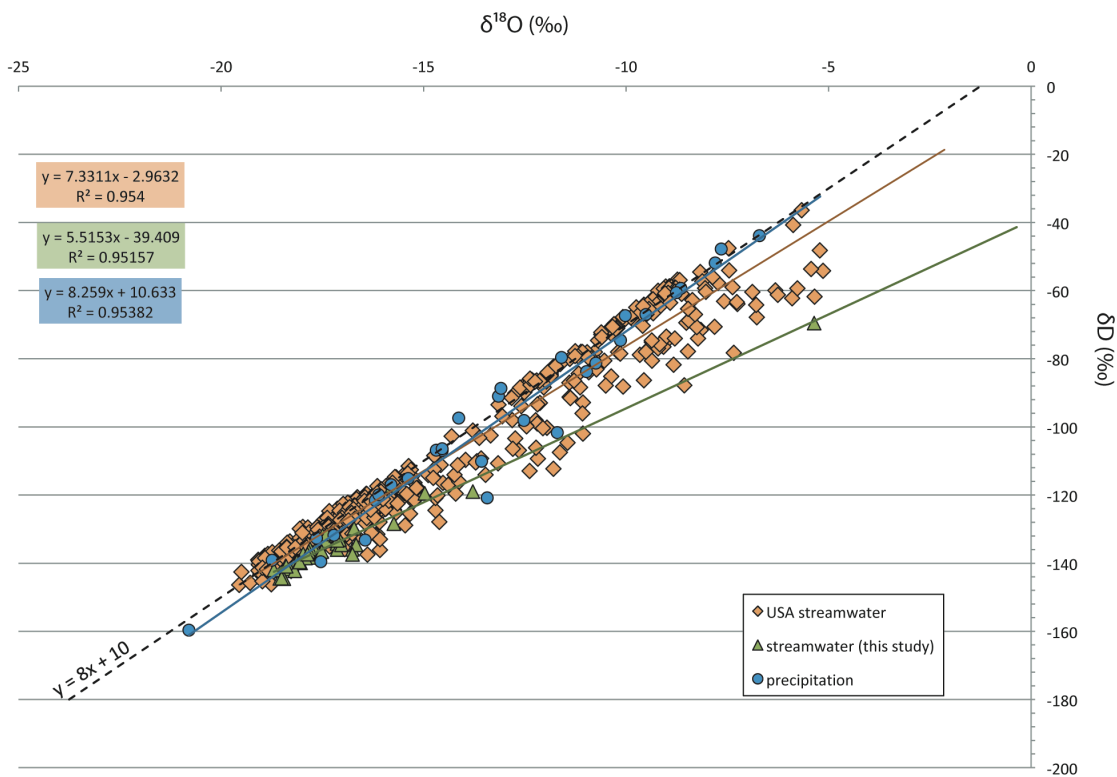**Figure A1.** Plot of $\delta^{18}O$ vs. δD of modern stream (diamonds) and precipitation (circles) waters at ~45°N latitude. Stream waters analyzed for this study are denoted by triangles. Trendlines reflect meteoric water lines for three subsets of data. Data from this study, Waterisotopes Database (2020), and IAEA/WMO (2021).
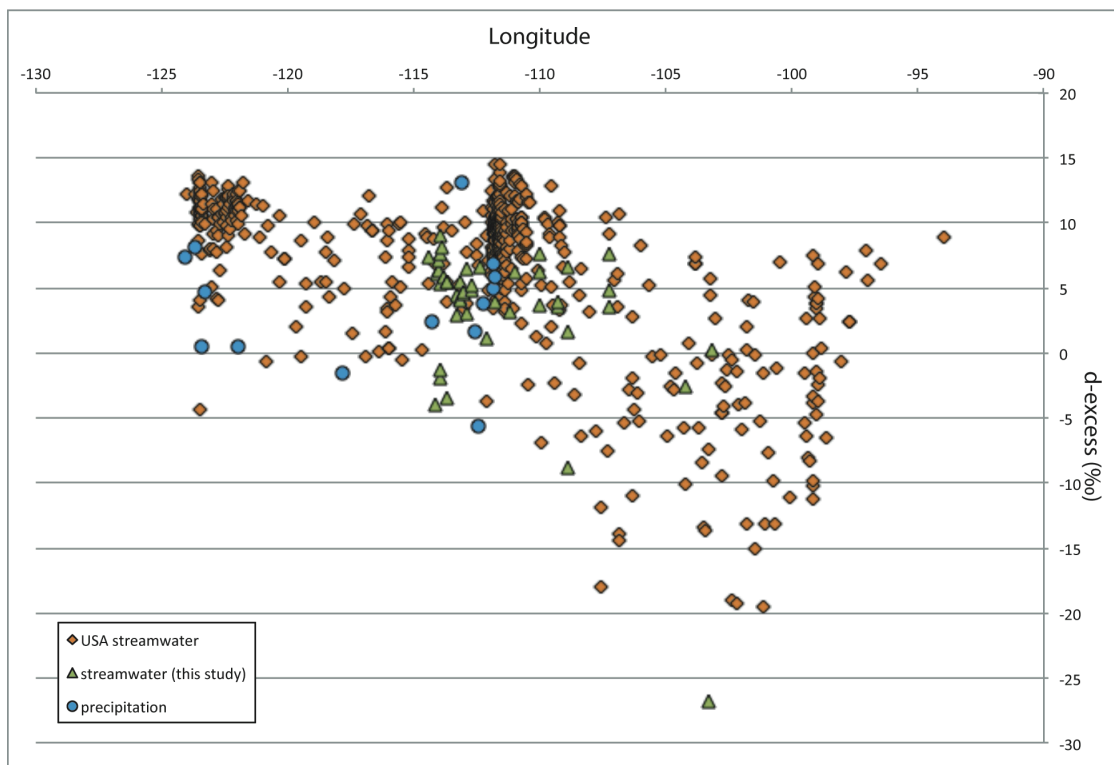
Figure A2. Plot of longitude vs. d-excess of modern stream (diamonds and triangles) and precipitation (circles) waters at ~45°N latitude. Stream waters analyzed for this study are denoted by triangles. Data from this study, Waterisotopes Database (2020), and IAEA/WMO (2021).
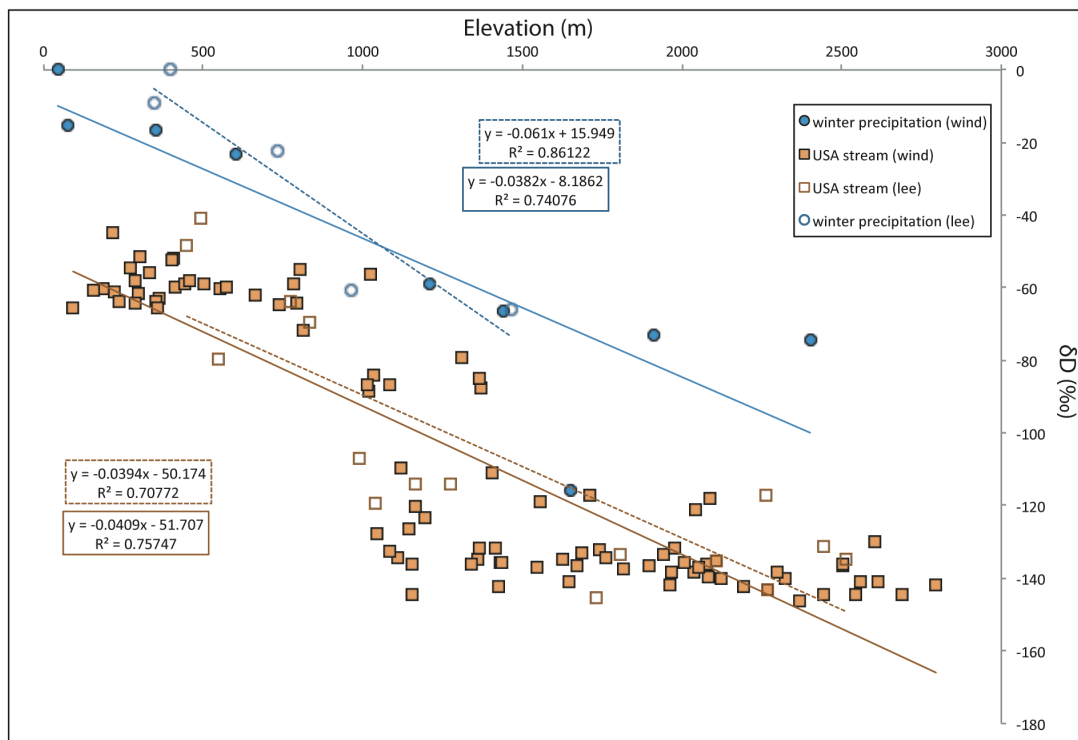
Figure A3. Plot of elevation vs. δD of modern stream (diamonds) and precipitation (circles) waters at ~45°N latitude. Trendlines reflect lapse rates for stream and precipitation waters on windward and leeward sides of the Rockies. Data taken along ~45°N transect from Waterisotopes Database (2020), and IAEA/WMO (2021).